



Distributed Low Temperature Combustion 133024

Peter Lindstedt
IMPERIAL COLLEGE OF SCIENCE TECHNOLOGY & MEDICINE

09/07/2016
Final Report

DISTRIBUTION A: Distribution approved for public release.

Air Force Research Laboratory
AF Office Of Scientific Research (AFOSR)/ IOE
Arlington, Virginia 22203
Air Force Materiel Command

REPORT DOCUMENTATION PAGE				Form Approved OMB No. 0704-0188	
<p>The public reporting burden for this collection of information is estimated to average 1 hour per response, including the time for reviewing instructions, searching existing data sources, gathering and maintaining the data needed, and completing and reviewing the collection of information. Send comments regarding this burden estimate or any other aspect of this collection of information, including suggestions for reducing the burden, to Department of Defense, Executive Services, Directorate (0704-0188). Respondents should be aware that notwithstanding any other provision of law, no person shall be subject to any penalty for failing to comply with a collection of information if it does not display a currently valid OMB control number.</p> <p>PLEASE DO NOT RETURN YOUR FORM TO THE ABOVE ORGANIZATION.</p>					
1. REPORT DATE (DD-MM-YYYY) 07-09-2016		2. REPORT TYPE Final		3. DATES COVERED (From - To) 01 Feb 2013 to 31 Jul 2016	
4. TITLE AND SUBTITLE Distributed Low Temperature Combustion: Fundamental Understanding of Combustion Regime Transitions				5a. CONTRACT NUMBER	
				5b. GRANT NUMBER FA8655-13-1-3024	
				5c. PROGRAM ELEMENT NUMBER 61102F	
6. AUTHOR(S) Peter Lindstedt				5d. PROJECT NUMBER	
				5e. TASK NUMBER	
				5f. WORK UNIT NUMBER	
7. PERFORMING ORGANIZATION NAME(S) AND ADDRESS(ES) IMPERIAL COLLEGE OF SCIENCE TECHNOLOGY & MEDICINE EXHIBITION RD LONDON, SW7 2BT GB				8. PERFORMING ORGANIZATION REPORT NUMBER	
9. SPONSORING/MONITORING AGENCY NAME(S) AND ADDRESS(ES) EOARD Unit 4515 APO AE 09421-4515				10. SPONSOR/MONITOR'S ACRONYM(S) AFRL/AFOSR IOE	
				11. SPONSOR/MONITOR'S REPORT NUMBER(S) AFRL-AFOSR-UK-TR-2016-0021	
12. DISTRIBUTION/AVAILABILITY STATEMENT A DISTRIBUTION UNLIMITED: PB Public Release					
13. SUPPLEMENTARY NOTES					
14. ABSTRACT <p>The objective of the current study is to bring fundamental understanding of the impact of the chemical (τ_c) and flow (τ_f) timescales on combustion regime transitions in turbulent premixed flows. Hence, τ_c is here varied via the mixture stoichiometry (ϕ) with variations in τ_f pursued in a parallel study. Aerodynamically stabilised dimethyl ether (DME) flames in a backstep burnt opposed jet configuration, featuring fractal generated multi-scale turbulence ($Re_t > 350$), are used to study decoupled parameters affecting τ_c and combustion regime transitions from conventional flamelets into the distributed reaction zone regime. The choice of DME is partly due to the potential practical relevance, but also due to the fundamentally different chemical behaviour as compared to ethanol. The latter fuel has also been considered along with methane. Work has also been performed on the further assessment of chemical mechanisms for the considered fuels (e.g. DME) to establish their ability to reproduce laminar flame and auto-ignition properties. The chemical mechanisms were then used to determine parameters required in the estimation of the different Damkoehler numbers. This chemistry can be used to identify the impact of the major chemical pathways on combustion mode transitions. The conceptual multifluid approach of Spalding can be used to avoid the limitations associated with the common bimodal (two-fluid) description and is here explored via simultaneous OH-PLIF and PIV, permitting the identification of five separate fluid states.</p>					
15. SUBJECT TERMS EOARD, Low Temperature Combustion, Combustion Regime Transitions					
16. SECURITY CLASSIFICATION OF:			17. LIMITATION OF ABSTRACT SAR	18. NUMBER OF PAGES 75	19a. NAME OF RESPONSIBLE PERSON CUMMINGS, RUSSELL
a. REPORT Unclassified	b. ABSTRACT Unclassified	c. THIS PAGE Unclassified			19b. TELEPHONE NUMBER (Include area code) 011-44-1895-616021

Final Report FA8655-13-1-3024

Distributed Low Temperature Combustion: Fundamental Understanding of Combustion Regime Transitions

Period of Performance: 1 February 2013 to 31 July 2016

*F. Hampp, P. Kraus, P. Simatos and R. P. Lindstedt**
Department of Mechanical Engineering, Imperial College,
Exhibition Road, London SW7 2AZ, UK

*Principal Investigator, email: p.lindstedt@imperial.ac.uk

Contents

1	Introduction	8
2	Methods, Assumptions, and Procedures	9
2.1	Multi-Fluid Description	11
2.2	Classification of the Multiple Fluid States	12
2.2.1	Density Segregation Technique	12
2.2.2	Fluid Detection using OH-PLIF	13
2.2.3	Hot Combustion Products	13
2.2.4	Mixing/Preheat (Low Temperature Chemistry) Fluids	14
2.2.5	Strongly Reacting Fluid	14
2.2.6	Product Fluid	15
2.2.7	Mildly Reacting Fluid	16
2.3	Sensitivity Analysis	17
2.4	Spatial Multi-Fluid Resolution	17
3	Results and Discussion	18
3.1	Multi-Fluid Analysis	18
3.2	Unconditional Velocity Statistics	20
3.3	Conditional Velocity Statistics	20
3.3.1	Conditional Reactant Fluid Velocity	21
3.3.2	Conditional Mixing Fluid Velocity	21
3.3.3	Conditional Mildly Reacting Fluid Velocity	22
3.3.4	Conditional Strongly Reacting Fluid Velocity	22
3.3.5	Conditional Strain Distribution on Material Surfaces	22
3.3.6	Strain Distribution along the Reactant Fluid Surface	23
3.3.7	Strain Distribution along Chemically Active Fluid Surfaces	23
3.4	Bimodal Flow Analysis	24
3.5	Impact of Excess Enthalpy on the Burning Mode Transition	25
3.5.1	Multi-Fluid Probability Statistics	25
3.5.2	Conditional Velocity Statistics	26
3.5.3	Conditional Strain along Material Surfaces	27
3.6	Combustion Regime Transitions	28
3.7	Calculation Methods for Distributed Combustion Regimes	30
3.7.1	Efficiency Gains from Parallelisation	32
4	Conclusions	33
5	Acknowledgements	35
6	References	35

7	Tables	42
8	Figures	46

List of Figures

1	Experimental configuration	47
2	Coordinate system convention and reference windows	47
3	Identification of the multiple fluid states in a sample Mie scattering and OH-PLIF image.	48
4	Schematic visualisation of the multi-fluid post-processing methodology. .	49
5	OH concentration following mixing of cold air with HCP to establish the maximum OH signal levels in the absence of fuel.	50
6	Theoretical mixture seeding density due to UN and LN stream mixing as a function of blending quantity (i.e. mixing temperature) and seeding density ratio for and HCP temperature = 1700 K.	51
7	DME auto-ignition delay times.	51
8	Laminar flame calculations to determine the extinction strain and to define the strongly reacting fluid threshold.	52
9	Laminar flame calculations to visualise the change in burning mode with increasing strain in the back-to-burnt configuration for premixed DME/air flames at varying Φ	53
10	Laminar flame calculations in a BTB geometry for varying HCP conditions.	54
11	OH lifetime in the post combustion environment for DME at $\Phi = 0.60$, 0.80 and 1.00 under extinction conditions.	55
12	Sensitivity analysis on the fluid separating threshold values for varying Φ .	55
13	Example of a quinary multi-fluid field.	56
14	Multi-fluid probability statistics for DME cases at $\Phi = 0.2 - 1.0$ aligned at the first thermal alteration iso-contour.	57
15	Multi-fluid interface diagrams for DME/air mixtures.	58
16	Unconditional mean axial velocity and axial and radial fluctuations along the burner centre axis.	59
17	Conditional mean axial reactant fluid velocity and fluctuations along the stagnation point streamline.	60
18	Conditional mean axial mixing fluid velocity and fluctuations along the stagnation point streamline.	61
19	Conditional mean axial mildly reacting fluid velocity and fluctuations along the stagnation point streamline.	62
20	Conditional mean axial strongly reacting fluid velocity and fluctuation along the stagnation point streamline.	63

21	PDF of the rate of strain and vorticity evaluated along the reactant fluid surface.	64
22	PDF of the rate of strain and vorticity evaluated along the mildly reacting fluid surface.	64
23	PDF of the rate of strain and vorticity evaluated along the strongly reacting fluid surface.	65
24	Coordinate system convention.	65
25	Multi-fluid probability for DME cases at $\Phi = 0.6$ with HCP temperature = 1600 – 1800 K.	66
26	Multi-fluid interface diagram for DME / air at $\Phi = 0.6$ and varying supporting HCP temperature.	67
27	Conditional mean axial mixing fluid velocity and fluctuations for varying HCP enthalpy along the stagnation point streamline.	68
28	Conditional mean axial mildly reacting fluid velocity and fluctuations for varying HCP enthalpy along the stagnation point streamline.	69
29	PDF of the rate of strain and vorticity evaluated along the reactant fluid iso-contour.	70
30	Combustion regime transitions of DME/air mixtures at varying Φ visualised in a Borghi diagram.	70
31	Auto-ignition manifold for DME/air mixtures.	71
32	The theoretical maximum speed-up according to Amdahl's Law [64].	72
33	The difference in memory alignment of a Structure of Arrays and Arrays of Structures.	72
34	Validating the MPI results using the serial code.	73
35	The achieved speed-up of PIPER using MPI.	73

List of Tables

1	Summary of utilised OH intensities for varying fuel and equivalence ratio to define the fluid separating thresholds.	43
2	Summary of turbulent and chemical conditions to derive the turbulent Reynolds, Damköhler and Karlovitz numbers for DME/air mixtures at varying Φ and low rate of strain.	43
3	Summary of utilised OH intensities for DME/air at $\Phi = 0.6$ and varying HCP temperature to define the fluid separating thresholds.	44

4	Summary of turbulent and chemical conditions to derive the turbulent Reynolds, Damköhler and Karlovitz numbers for DME/air at $\Phi = 0.6$ and varying HCP enthalpy.	44
5	Physical and resolved length scales in μm . λ_{PIV} and λ_{MF} is the PIV and multi-fluid resolution, respectively. The current minimum laminar flame thickness at $\Phi = 1.0$ is $\min(\delta_f)$. λ_D is the mean scalar dissipation layer thickness [59] and λ_B the Batchelor scale [60].	44
6	Multi-fluid interface probabilities for DME/air mixtures by traversing along the stagnation point streamline.	45
7	Multi-fluid interface probabilities for varying HCP enthalpy by traversing along the stagnation point streamline.	45

Summary

The objective of the current study is to bring fundamental understanding of the impact of the chemical (τ_c) and flow (τ_f) time-scales on combustion regime transitions in turbulent premixed flows. Hence, τ_c is here varied via the mixture stoichiometry (Φ) with variations in τ_f pursued in a parallel study. Aerodynamically stabilised dimethyl ether (DME) flames in a back-to-burnt opposed jet configuration, featuring fractal generated multi-scale turbulence ($Re_t \geq 350$), are used to study decoupled parameters affecting τ_c and combustion regime transitions from conventional flamelets into the distributed reaction zone regime. The choice of DME is partly due to the potential practical relevance, but also due to the fundamentally different chemical behaviour as compared to ethanol. The latter fuel has also been considered along with methane. Work has also been performed on the further assessment of chemical mechanisms for the considered fuels (e.g. DME) to establish their ability to reproduce laminar flame and auto-ignition properties. The chemical mechanisms were then used to determine parameters required in the estimation of the different Damköhler numbers. This chemistry can be used to identify the impact of the major chemical pathways on combustion mode transitions. The conceptual multi-fluid approach of Spalding can be used to avoid the limitations associated with the common bimodal (two-fluid) description and is here explored via simultaneous OH-PLIF and PIV, permitting the identification of five separate fluid states. The latter are defined as reactant, combustion product, mixing, mildly reacting and strongly reacting (e.g. flamelet) fluids. To distinguish between the different chemically active fluids, thresholds are defined based on the detected OH signal. The sensitivity of the distribution between the different fluid states to the threshold values is also evaluated. In order to correlate the fluid state thresholds to their physical interpretation, laminar flame calculations in the directly corresponding geometry were carried out. The work suggests that a consistent treatment of applied threshold levels is necessary when comparing different types of simulations (e.g. DNS) and experiments for reacting fluids with multiple states. However, the work also suggests that such characterisations are possible and useful in delineating combustion regime transitions. The application of calculation methods that do not rely on a presumed (e.g. flamelet) structure requires the introduction of multiple chemical time-scales. To this effect, the scope of parallelising the treatment of the chemistry in the context of transported joint-*pdf* methods has also been explored on different platforms in order to permit effective computations featuring extended mechanisms for practical fuels. The latter are of a size approaching that of mechanisms based on the rapid decomposition hypothesis leading to the C_1 – C_2 and/or C_1 – C_4 foundation chemistry. It is shown that close to the theoretical maximum speed-up can be achieved.

1 Introduction

Combustion technologies operating in the absence of distinct flame fronts are expected to lead to improved control, reduced fuel consumption through stable fuel lean operation, low maximum temperatures and reduced emissions. This development induces the need to extend laboratory research to significantly higher turbulence levels and reduced Damköhler numbers to provide fundamental understanding of combustion regime transitions including distributed and/or flameless regimes, e.g. flameless oxidation (FLOX) [1, 2], high temperature air combustion (HiTAC) [3] or moderate and intense low oxygen dilution (MILD) combustion [4, 5]. The opposed jet geometry has been extensively utilised to investigate turbulent (and laminar) non-premixed, partially premixed and premixed combustion as well as, more recently, regime transitions [6, 7, 8, 9]. The geometry entails decisive advantages rendering it indispensable for experimental combustion studies as well as computational model development and validation [10, 11]. These are: (i) Excellent optical access for laser-based diagnostic measurements; (ii) Accurate experimental control of boundary conditions; (iii) Aerodynamic flame stabilisation, rather than through pilot flames, leading to flame dynamics and extinction being directly related to the intrinsic aerothermochemistry of the combustion process; (iv) Individual control of variables affecting the chemical and turbulent time-scale and (v) a compact physical domain ideal for LES and other computational studies. The last three points identify the current experimental facility as arguably ideal for investigations of combustion regime transitions.

Dimethyl ether (DME) has been promoted since the mid-1990s [12, 13] as an attractive alternative to Diesel. Numerous investigations are found on the utilisation of DME in engines, e.g. [14, 15], yet fundamental flame studies are relatively rare. Existing studies have investigated properties such as laminar burning velocities [16, 17, 18] and extinction strain rates [18]. Recently, Fuest et al. [19] presented an experimental study of laminar and turbulent DME jet flames using Raman/Rayleigh scattering and CO-LIF supported by laminar flame calculations. Species and temperature profiles were obtained for two equivalence ratios and good agreement was found between experiment and computation. Furthermore, a higher impact of differential diffusion was established for all DME/air flames compared to CH_4 /air flames due to significantly increased level of molecular hydrogen. Gabet et al. [20] compared the flame structure of non-premixed DME and CH_4 / air turbulent jet flames. Despite the increasing number of publications, no research effort with respect to the combustion regime transition of premixed DME/air flames has been found in literature. The latter issue is partially addressed in the current study by considering data that may permit an extension of arguably the most successful statistical description of turbulent premixed combustion, i.e. the two-fluid BML model [21]. The work performed on DME

is here used as an example of the investigations performed. In addition, methane [22, 23] and ethanol [23] have also been considered.

The statistical description of combustion approaching distributed reaction zones necessitates a more complex methodology as significant reaction zone broadening and intermediate fluid states are expected. Consequently, the current work utilises a back-to-burnt (BTB) opposed jet configuration to investigate the impact of the chemical timescale and excess enthalpy on the combustion regime transition of lean premixed DME flames. The conceptual multi-fluid approach of Spalding [25] is explored via simultaneous OH – PLIF and PIV permitting the identification of various combustion gas states. A range of Damköhler numbers (Da) from the conventional propagating flamelet regime well into the distributed reaction zone regime are investigated. The latter requires the application of calculation methods that do not rely on a presumed (e.g. flamelet) structure and inevitably leads to the need to introduce multiple chemical time-scales. The scope of parallelising the treatment of the chemistry in the context of transported *joint-pdf* methods has accordingly been explored in order to permit effective computations featuring extended mechanisms for practical fuels. The latter are of a size approaching that of mechanisms based on the rapid decomposition hypothesis leading to the C_1 – C_2 and/or C_1 – C_4 foundation chemistry [26].

2 Methods, Assumptions, and Procedures

Combustion regime transitions from self-sustained flames (e.g. flamelets) to distributed reactions can be achieved by augmenting the turbulence intensity or by slowing down the combustion chemistry. In the present work, burning mode transitions were systematically enforced by altering the chemical timescale via the mixture stoichiometry ($0.0 < \Phi < 1.0$), while maintaining τ_I constant with $Re_t \geq 350$ ($Re \simeq 18,400$). This corresponds to conditions beyond the intense turbulence regime $u_{rms}/S_L \simeq 19$ [27] with the present values covering the range $3.3 \leq u_{rms}/S_L \leq 43$. Zhou et al. [28] identified distributed reactions in stoichiometric vitiated CH_4 jet flames for $Re_t > 240$, which reduced to $Re_t > 130$ for $\Phi = 0.4$. The impact of the excess enthalpy of the supporting HCP stream on the regime transition is also investigated. Based on a conventional combustion regime diagram [29, 30] the conditions cover a transition from (close to) corrugated flamelets to distributed reaction zones.

The multi-fluid concept of Spalding [25] is explored via simultaneous Mie scattering, particle image velocimetry (PIV) and hydroxyl planar laser induced fluorescence (OH-PLIF) in order to extend bimodal (two-fluid) approaches [21]. This novel analysis permits the statistical evaluation of intermediate fluid states that are found in low Damköhler number flows. The current implementation allows segregations of five different fluid states

(reactants, combustion products, mixing fluid, mildly and strongly reacting fluids), with a thermochemical interpretation provided. The derived multi-fluid analysis is here used to delineate systematic combustion regime transitions from close to the corrugated flamelet regime well into a distributed reaction zone regime of premixed DME by means of (a) multi-fluid probability and (b) interface statistics, (c) unconditional and (d) conditional velocity statistics, (e) underlying strain statistics conditioned upon the material surfaces and (f) limitations of bimodal segregation techniques. The multi-fluid analysis is further used to delineate (g) the impact of the excess enthalpy of the stabilising hot combustion product on the burning mode transition with the impact of the fuel chemistry explored by Hampp [22] and strain (bulk and turbulent) by Hampp and Lindstedt [24]. The conventional combustion regime classification is extended by (h) a tentative delineation into a 3D regime manifold to accommodate conditions of distributed burning modes.

The opposed jet burner (Fig. 1), originally developed by Geyer et al. [11], was extensively used by Geipel et al. [10] and Goh et al. [8, 31, 32, 33] and is identical to the configuration used by Hampp et al. [22, 23]. A cross fractal grid (CFG; [34]) was installed 50 mm upstream the UN exit, featuring a BR of 65 % with maximum and minimum bar widths of 2.0 mm and 0.50 mm. The CFG provides increased multiscale turbulence [8, 10, 31, 32]. Premixed DME / air mixtures with $U_{b,UN} = 11.0$ m/s at $T_{UN} = 320$ K were injected through the upper nozzle (UN) at varying $\Phi = 0.20, 0.40, 0.60, 0.80$ and 1.0 . The velocity fluctuations ($u_{rms} = 1.58$ m/s) and the integral length scale of turbulence ($L_I = 4.1$ mm) were measured using hot wire anemometry, resulting in a turbulent Reynolds number of $Re_t \approx 370$ (with kinematic viscosity (ν) of $17.9 \cdot 10^{-6}$ for air at 320 K).

Premixed H_2 ($\Phi = 1.0$) flames were stabilised on a stabilising mesh (FSM), located 100 mm upstream the LN exit, providing thermally equilibrated hot combustion products (HCP) to the stagnation plane. A flashback arrestor (FBA) is installed for safety. The HCP temperature was controlled by the CO_2 dilution rate within the range of 1600 to 1800 K. The nozzle exit temperature and its peak-to-peak variation of ~ 1 % were measured using an R-type thermocouple with an estimated time constant of 10 ms. The aerodynamic stabilisation of the stagnation plane in the proximity of the burner centre (mid-point between the nozzles) was realised by matching the momentum of the LN HCP stream and the UN premixed fuel-air mixture. Thus, the target Re_t necessitated a LN bulk velocity of $U_{b,LN} \approx 4.3$ m/s (at 293 K). The coordinate system convention is shown in Fig. 2.

Simultaneous OH – PLIF and PIV were carried out using the $Ba(NO_3)_2$ crystal based Raman laser of Kerl et al. [35] (two light sheets; 281.7 nm and 532 nm; height = 1D; thickness < 0.5 mm; $\Delta t = 25$ μs). The OH – PLIF images were obtained from the first laser pulse. The interrogation regions for the OH – PLIF and PIV cameras were set to

51.9×38.6 mm and 34.5×25.6 mm (1376×1023 pixels). Aluminium oxide (Al_2O_3) powder ($\rho_a = 3900 \text{ kg/m}^3$), with particle diameters of $d_{a,50} = 0.44 \text{ }\mu\text{m}$ and $d_{a,90} = 1.66 \text{ }\mu\text{m}$, was used as velocity tracer particles. Adaptive PIV with decreasing interrogation window sizes (128×128 to 48×48 with a 75 % overlap) offers the highest accuracy, spatial resolution and robustness at the penalty of significantly increased calculation time [36]. The determined velocity field is resolved by 115×88 vectors, providing a spatial resolution of 0.30 mm. The experimental and diagnostic setup were discussed in detail by Hampp et al. [22, 24].

2.1 Multi-Fluid Description

Combustion with $\text{Da} < 1$ can lead to a broadening of reaction zones as observed in vitiated jet flames [37, 38, 28, 39] and DNS [40, 41]. Burning modes with distributed reactions show a strong degeneration of the laminar species / reaction progress correlation [41] and a bimodal two-fluid description (reactants and products) with a negligible probability of encountering chemically active states becomes problematic [42]. Spalding [25] suggested a multi-fluid approach that permits the identification of various intermediate fluid states. The concept was explored by Hampp [22] and Hampp and Lindstedt [23, 24] using simultaneous Mie scattering, PIV and OH – PLIF combined with a purpose written algorithm (summarised see below) that detects four iso-contours in each instantaneous image pair in order to distinguish between five different fluid states. The existence of relatively rare events required 3000 independent realisations to maintain statistical accuracy.

The experimentally observed OH signal intensity bands were linked to theoretically determined OH concentrations to provide physical interpretation. Three types of calculations were performed with the chemical reaction mechanism of Park [43].

1. Freely propagating laminar flames calculations replicated the experimental conditions of the lower in-nozzle flow and provided a value for the OH radical concentration at the LN exit that is used as reference ($[\text{OH}^\ddagger]_T$). The measured nozzle exit temperature was matched via a radiation heat loss correction [44] of 7.2 – 8.9 %. The computational domain was resolved by 660 distributed cells with local refinement of the reaction zone.
2. One-dimensional strained laminar flame calculations [44] were performed in the twin flame mode to determine the flame extinction point and in the BTB mode corresponding to the experimental configuration to provide a consistent set of Da for all conditions. The computational domain was resolved by 390 distributed cells with local refinement of the CH peak leading to a resolution $< 12 \text{ }\mu\text{m}$.

3. Zero-dimensional shock tube calculations were carried out to determine auto-ignition delay times and perfectly stirred reactor (PSR) calculations to estimate OH lifetimes in different fluids. The time step of the PSR calculation was adjusted to resolve the ignition onset and was as low as 1×10^{-8} s for high T_0 .

The linking of experimental data, e.g. OH – PLIF signal levels, to theoretically determined radical concentrations via laminar flame calculations, to support post-processing strategies becomes essential when using the signal intensity of one reaction zone marker, e.g. OH – PLIF signal, to highlight differences within the intensity of the chemical activity.

2.2 Classification of the Multiple Fluid States

The selected thermochemical fluid states accessible with the used simultaneous Mie scattering, PIV and OH – PLIF technique are defined below and sample images with overlaid PIV vectors and detected iso-contours are shown in Fig. 3. The overall flow chart to determine the different fluid states is depicted in Fig. 4.

Reactant Fluid: Fresh reactants emerging from the UN that have not undergone thermal alteration (i.e. oxidation or mixing processes) are detected via density segregation.

Mixing Fluid: A fluid state without detectable OH signal that has been exposed to a thermal change (i.e. mixing of HCP with reactants).

Mildly Reacting Fluid: A fluid state with modest levels of OH such as the chemical activity of ultra lean flames that are sustained by the thermal support provided by an external enthalpy source.

Strongly Reacting Fluid: Regions with a strong OH signal intensity indicate a large OH radical pool that originates from self-sustained (e.g. flamelet) burning and conventional aerothermochemistry conditions and extinction criteria apply [45].

Product Fluid: Burnt combustion products (BCP) from the UN mixture are combined with HCP from the LN.

2.2.1 Density Segregation Technique

PIV tracer particle based density segregation (DS) techniques are widely used, e.g. [31, 46, 47], and the current methodology is a variant that enables the detection of more general flow structures. The DS iso-contour is determined based on a binary image via Moore-Neighbor tracing with a Jacobs stopping criteria [48]. The algorithm permits the detection of multiple, fragmented and disconnected zones. Mixing of the opposing streams

and subsequent heat release can result in ambiguous determinations and constraints were imposed on the seeding densities (N_{sd}). To achieve unambiguous signal identification $N_{sd,UN} \geq 1.75 \cdot N_{sd,LN}$ was found sufficient to ensure a unique density segregation iso-contour. Over-seeded images were rejected as heat release associated changes of $N_{sd,UN}$ could not be detected due to pixel saturation. The overall rejection rate was $< 5 \%$.

2.2.2 Fluid Detection using OH-PLIF

The experimentally determined OH signal intensities were linked to theoretical OH radical concentrations in order to segregate different reactive fluid states. Alternative methods are possible by using other chemical species (e.g. CH or CH₂O). However, with increasing reaction zone broadening, the CH₂O and OH layers are expected to penetrate further into the zone of maximum heat release (CH peak) [38], potentially improving the OH marker capabilities. Further, the current procedure has the benefit of simplicity and a sustained OH concentration ($[\text{OH}^\ddagger]_T$) in the HCP was used as reference level at a fixed location (dashed LN rectangle in Fig. 2). The peak-to-peak fluctuations of the LN exit temperature, i.e. $T_{HCP} \pm 1 \%$, translates to an uncertainty in the OH concentration of $\sim 7 \%$. The theoretically determined $[\text{OH}^\ddagger]_T$ concentrations for different T_{HCP} ($7.38 - 10.8 \times 10^{-3} \text{ mol/m}^3$) were combined with the corresponding experimental OH signal intensity I^\ddagger (normalised to unity) to delineate the other fluid state (FS) intensities ($I_{FS,\chi}$) via Eq. (1). For the current purpose a simple linear correlation between the fluorescence signal and OH concentration was found valid over a comparatively wide range ($1200 \leq T \text{ (K)} \leq 2200$) [22] with the used signal intensities listed in Table 1.

$$I_{FS,\chi} = \frac{[\text{OH}]_{FS,\chi}}{[\text{OH}^\ddagger]_T} \cdot I^\ddagger \quad (1)$$

2.2.3 Hot Combustion Products

The determined reference state ($[\text{OH}^\ddagger]_T$) is well defined. However, an experimentally observed OH surplus ($I > I^\ddagger$) was found in the mixing layer of an isothermal ($\Phi = 0.0$) case. The cause can readily be analysed by considering the mixing of HCP with air from the UN through PSR calculations featuring a residence time range covering the integral (τ_I) and Kolmogorov (τ_η) timescales. The OH radical is stable at the HCP conditions as shown by the normalised OH concentration in the far right of Fig. 5 for $T_{HCP} = 1600 - 1800 \text{ K}$. However, a decrease in temperature by means of cold air admixture results in a surging OH concentration, peaking at $T_0/T_{HCP} \approx 0.9$, followed by a decay. The excess OH concentration ($[\text{OH}] / [\text{OH}^\ddagger] > 1$) at low air blending ratios with (e.g. $T_0/T_{HCP} \geq 0.8$) results from the oxidation of the residual H₂ and CO in the HCP via O₂ from the

air stream [22]. At higher blending ratios the OH signal is increasingly quenched and vanishes around $T_0/T_{HCP} \approx 0.55$. The maximum increase in the OH concentration due to the blending of HCP gas and air is around 185 % and constant for all T_{HCP} . Using Eq. (1), $[\text{OH}]_{HCP,T}$ ($13.7 - 20.0 \times 10^{-3} \text{ mol/m}^3$) can be transformed into an expected OH signal intensity with $I_{HCP} = 1.85 \cdot I^\ddagger$, which is rounded to $2.0 \cdot I^\ddagger$ and subsequently used in Section 2.2.6 to define the product fluid threshold.

2.2.4 Mixing/Preheat (Low Temperature Chemistry) Fluids

Regions with a drop in seeding density of the UN stream (i.e. a thermal alteration of the fluid), but without a detected OH signal (i.e. no distinct chemical activity) were denoted as mixing fluid. The change in the seeding density (N_{sd}) is a consequence of the mixing of the UN reactant stream (high seeding density) with the LN hot combustion products as shown for $T_{HCP} = 1700 \text{ K}$ in Fig. 6. The seeding density ratio was varied between $1.75 \leq N_{sd,UN}/N_{sd,LN} \leq 100$. The lower limit follows from the minimum seeding density ratio requirement while the upper limit is set by the ratio of saturation to background signal of the camera. An estimated HCP blending fraction of $5 \pm 2 \%$ by volume, depending on the seeding density ratio (see Fig. 6), with cold reactants is sufficient to detect the thermal alteration. An estimated cold gas addition of $40 \pm 10 \%$ is effective to quench of the OH radical concentration in the HCP. Refinements in the upper limit definition are possible if there is a desire to identify regions of low temperature chemistry (e.g. characterised by CH_2O). Computations of auto-ignition delay times, defined by the steepest temperature gradient (Fig. 7), suggest that a residence time of one integral timescale corresponds to an auto-ignition temperature $T_{ign} \approx 1200 \text{ K}$ that is relatively independent of Φ .

2.2.5 Strongly Reacting Fluid

At high Damköhler numbers, vigorously burning flames detach from the stagnation plane and conventional aerothermochemical conditions apply. To provide a physical interpretation, theoretical OH concentrations for the strongly reacting fluid were correlated with a self-sustained burning mode for each equivalence ratio via laminar flame calculations [44].

Chemical Timescale Variation The peak OH concentration at the extinction point of strained counterflow twin flames provides a reference point for the lowest expected OH concentration of self-sustained burning ($[\text{OH}]_{str,\chi}$) [22]. The OH peak at extinction ($a_{q,\Phi}$) is used to mark a lower limiting OH concentration ($[\text{OH}]_{str,\chi}$) for each Φ as shown in Fig. 8. This specifies an approximate threshold ($\Lambda_{OH,str,\chi}$), above which self-sustained

burning in absence of HCP support is possible. The determined OH concentration under extinction condition is related to the reference level ($[\text{OH}^\ddagger]_T$) by Eq. (2).

$$\begin{aligned}\Lambda_{OH, str, \chi} &= \frac{[\text{OH}]_{str, \chi}}{[\text{OH}^\ddagger]_T} \leq \frac{I_{str, \chi}}{I^\ddagger} \\ I_{str, \chi} &\geq \Lambda_{OH, str, \chi} \cdot I^\ddagger\end{aligned}\quad (2)$$

The observed rates of strain, discussed in Section 3.3.5, prevent self-sustained burning for mixtures below the lower flammability limit and thus the definition of $[\text{OH}]_{str, \chi}$ is not meaningful for $\text{Da}_1 < 1$ ($\text{Da}_1 = (L_I \cdot S_L) \cdot (\delta_f \cdot u_{rms})^{-1} = \tau_I \cdot \tau_c^{-1}$). Calculations were accordingly also performed in a back-to-burnt (rather than twin-flame) configuration to infer the corresponding laminar burning velocity and flame thickness (see Figs. 9) values required to estimate the conventional flame property based Da_1 . The extinction strain rates (a_q) can be compared with the estimated turbulent strain $a_I \approx 3950 \text{ s}^{-1}$ and the determined normal a_n and tangential a_t strain along the material surfaces (see Section 3.3.5). Hence, it is expected that the HCP will exert some influence on all cases. Threshold values are summarised in Table 1 and extinction conditions are listed in Table 2.

HCP Temperature Variation The impact of the T_{HCP} on the burning mode is investigated for the case marking the transition from the thin reaction zone to distributed reactions, i.e. $\Phi = 0.6$, with an adiabatic flame temperature of $T_{ad} \simeq 1750 \text{ K}$, $S_L = 0.21 \text{ m s}^{-1}$ and $\delta_f = 0.46 \text{ mm}$. The equilibrium OH concentration in the HCP increases from 7.38×10^{-3} to $10.8 \times 10^{-3} \text{ mol/m}^3$ with T_{HCP} . The threshold value are altered accordingly as defined in Eq. (2) and listed in Table 3. The effect of T_{HCP} on corresponding laminar flames is shown in Fig. 10 by means of BTB calculations at varying rates of strain. For high HCP temperatures, δ_f reduces steadily by 30 % with increasing strain compared to the unstrained value as depicted in Fig. 10a. By contrast, at low T_{HCP} ($= 1600 \text{ K}$) δ_f initially increases for $a < 1000 \text{ s}^{-1}$ by $\sim 20 \%$ and subsequently reduces due to the increase in bulk strain. For high T_{HCP} , the S_L (Fig. 10b) and $[\text{OH}]_{peak}/[\text{OH}^\ddagger]_T$ (Fig. 10c) reduce until $a \leq 2500 \text{ s}^{-1}$ and are maintained constant for higher rates of strain. At reduced T_{HCP} both values plummet for $a \leq 1000 \text{ s}^{-1}$ and subsequently remain constant. The Da_1 is maintained constant at approximately 1.2 for high T_{HCP} , but reduces significantly to $\text{Da}_1 \simeq 0.3$ for low T_{HCP} as shown in Fig. 10d. The resulting global conditions are summarised in Table 4.

2.2.6 Product Fluid

The product fluid threshold is based on the maximum OH concentration in the HCP and the burnt combustion products (BCP) resulting from combustion of the UN reactants. The

OH concentration of the HCP ($[\text{OH}]_{HCP,T}$) is reliant upon the T_{HCP} , see above, while the OH concentration in the BCP ($[\text{OH}]_{BCP,\Phi}$) varies with the equivalence ratio and residence time. The lifetime of the OH radical in the BCP was estimated using perfectly stirred reactor simulations, see Fig. 11, with the residence time varied between the estimated Kolmogorov (τ_η) and the integral timescales.

The OH concentration decays to levels $\leq [\text{OH}]_{HCP,T}$ (i.e. $2.0 \cdot [\text{OH}^\ddagger]_T$) within $3.0 \cdot \tau_\eta$ (the multi-fluid resolution see Sec. 2.4) for DME at $\Phi = 0.60$, see Fig. 11. For all mixtures, the OH concentrations decay to values close to $[\text{OH}]_{HCP}$ within one integral timescale. The comparatively rapid decay suggests that a simple analysis approach is adequate for the current purposes. Accordingly, values corresponding to the small scale mixing processes ($3.0 \cdot \tau_\eta$) were used to estimate BCP signal intensities in comparatively fresh products as summarised in Tables 1 and 3. The combined value was selected as $[\text{OH}]_{prod,\chi} = \max([\text{OH}]_{HCP,T}, [\text{OH}]_{BCP,\Phi})$. The product fluid threshold ($\Lambda_{OH,prod,\chi}$) and the corresponding OH signal intensity ($I_{prod,\chi}$) were defined via Eq. (3).

$$\Lambda_{OH,prod,\chi} = \frac{[\text{OH}]_{prod,\chi}}{[\text{OH}^\ddagger]_T} \quad (3)$$

$$I_{prod,\chi} \leq \Lambda_{OH,prod,\chi} \cdot I^\ddagger$$

2.2.7 Mildly Reacting Fluid

Regions with modest OH signal levels can stem from (i) ignition events, (ii) the decay of OH concentration in combustion products or (iii) chemically active material that is diluted and sustained by HCP. Such regions are not further delineated and are denoted as mildly reacting fluid. The OH concentrations at the extinction point ($[\text{OH}]_{str,\chi}$) for twin flames were found to define the onset of a characteristic switch in the BTB burning mode and justify the implementation of the mildly reacting fluid into the multi-fluid analysis. The change is evident for the laminar flame thickness and laminar burning velocity as shown in Fig. 9 and defines a characteristic strain ($a_{c,\Phi}$). At higher rates of strain ($a > a_{c,\Phi}$), the maximum OH concentration, δ_f and S_L collapse and become insensitive to the reactant mixture composition. This implies that the flame is governed by the HCP and the OH concentration and experimental intensities for the mildly reacting fluid state are defined as:

$$\Lambda_{OH,prod,\chi} < I_{mild,\chi} < \Lambda_{OH,str,\chi} \quad (4)$$

The threshold values and intensity levels are summarised in Tables 1 and 3 and the sensitivity of the probability distribution to the threshold values is discussed below.

2.3 Sensitivity Analysis

The impact of thresholds on statistics was explored using a sensitivity analysis for the case close to a transition from the thin reaction zone regime to distributed reaction ($\Phi \geq 0.60$). Potentially, such cases are the most difficult to quantify. The spatial coordinate for the data is normalised by the integral length scale of turbulence and aligned on the iso-contour x_s that corresponds to the first thermal change noted in the Mie scattering data.

The product fluid threshold $\Lambda_{OH,prod,\Phi=0.6}$ separating combustion products from the mildly reacting fluid was varied between 1.6 – 2.4. The range starts below the uncertainty (~ 1.8) associated with oxidation of the residual HCP products. The overall variation is similar to the change ($\sim 30\%$) in the OH concentration of the twin $\Phi = 0.80$ flame moving from near unstrained conditions ($a = 75\text{ s}^{-1}$) to the extinction point ($a_q = 2000\text{ s}^{-1}$). Thus the threshold variation is substantial. Results shown in Fig. 12a highlight a reduction of the peak probability of the mildly reacting fluid, yet the spatial extent and general trend of the distribution is preserved. A value $\Lambda_{OH,prod,\Phi \leq 0.6} = 2.0$ is preferred as the lower bound (see Section 2.2.6).

The sensitivity of the strongly reacting (flamelet) burning mode probability was investigated by applying a threshold variation from below the extinction OH concentration in the twin flame configuration with a symmetric shift around the defined thresholds, i.e. $3.0 < \Lambda_{OH,str,\Phi=0.6} < 3.8$. Translating the corresponding OH variation into the BTB configuration, the inferred strain rate range includes the region of characteristic change in the laminar flame thickness and laminar burning velocity depicted in Fig. 9. The results of the sensitivity analysis are shown in Fig. 12b. A reduction in peak probability is noted, while the spatial extent and distribution trend remains. The sensitivity can be expected due to the steep decay of the OH concentration around the extinction point. However, it is apparent that even with a large variation, the probability of finding chemically active fluid supported by HCP is around $36 \pm 11\%$ for the transitional case ($\Phi = 0.6$). The corresponding probability of finding strongly reacting (flamelet fluid) is $19 \pm 7\%$.

2.4 Spatial Multi-Fluid Resolution

The spatial (planar) resolution of the multi-fluid algorithm was determined by means of an USAF-1951 test target [50]. Due to the difference in applied smoothing filter width (i.e. 16 pixels for the Mie scattering image versus 4 pixels for the OH image) the spatial resolution of the multi-fluid analysis is limited by the detection algorithm of the Mie scattering iso-contour. Thus, an image of the resolution target was acquired with the Mie scattering camera and same post-processing / smoothing steps applied. The spatial (planar) resolution of the multi-fluid algorithm was determined to 0.25 mm, which corresponds to ~ 3

Kolmogorov length scales. Consequently, individual and instantaneous fluid states thinner than $3 \cdot L_\eta$ are disregarded. An overview of the spatial scales is provided in Table 5.

3 Results and Discussion

An example of a resulting quinary multi-fluid field, corresponding to the image pair in Fig. 3, is depicted in Fig. 13. The multi-fluid analysis is used to delineate combustion regime transitions of premixed DME/air flames with the chemical timescale varied by means of the mixture stoichiometry. The turbulence intensity is maintained constant at $Re_t \simeq 380$ with mixture specific details listed in Table 2. The change in burning mode from distributed reactions towards the corrugated flamelet regime is first evaluated by means of the (i) fluid state distribution and (ii) interface statistics with a Damköhler number (Da_1) variation, followed by turbulence-chemistry interaction through (iii) unconditional and (iv) conditional velocity statistics as well as (v) conditional velocity gradient statistics along the material surfaces. Subsequently, the impact of the HCP enthalpy on the burning mode transition is investigated. Last, a (vii) tentative classification of the burning mode transition is proposed in a 3D combustion regime manifold.

3.1 Multi-Fluid Analysis

The evolution and redistribution of the selected fluid states is discussed along the burner centre axis, i.e. stagnation point streamline (SPS), as a function of Da_1 . The results highlight the benefit of extending bimodal segregation techniques and include intermediate fluid states, in particular for low Da flows. Minor inconsistencies of the stagnation plane location may arise due to jet momentum matching. Hence, the spatial multi-fluid probabilities were aligned at the first thermal alteration of the fluid, i.e. $x_s = 0$, identified by the density segregation iso-contour. Inherently, the reactant fluid probability drops sharply from unity to zero at the origin as shown in Fig. 14a. However, it re-emerges downstream, extending to one integral length scale of turbulence with its peak at $\sim L_I/4$. The effect is independent of Da_1 and accordingly related to turbulent transport. The recurrence can be caused by large eddies tearing out pockets of unburnt reactants and/or a three-dimensional effects, yet remains $\leq 5\%$ for all cases.

The probability of finding mixing fluid is shown in Fig. 14b. A sharp rise at the origin provides evidence of the importance of this fluid state – particularly adjacent to the reactant fluid for flows with $Da_1 \leq 1.0$. At high reactivity, i.e. $\Phi = 1.0$, the peak probability of the mixing fluid in direct proximity of the origin is significantly reduced. This suggests an immediate onset of chemical activity adjacent to the reactant fluid, without the

necessity of HCP support. Moreover, with gradually increasing mixture reactivity the mixing fluid probability is reduced away from the origin in favour of chemical reactions, i.e. smaller quantities of HCP are required to initialise OH producing chemical activity. The results further show that the spatial extent of the mixing fluid is limited by L_I , suggesting a correlation with turbulent transport.

The probabilities of encountering regions with mildly and strongly reacting fluids were also estimated. With a decreasing chemical timescale the mildly reacting fluid (i.e. a fluid with $I_{mild,\Phi} < \Lambda_{OH, str, \Phi}$) gains significance as shown in Fig. 14c with the magnitude and spatial extent enhanced. The reduction in peak probability for mixtures with $Da_1 > 1.0$ is a consequence of the distinct augmentation of the strongly reacting (flamelet) fluid probability, see Fig. 14d. However, due to the comparatively high turbulence level, some impact of HCP support remains. The peak probability of the strongly reacting fluid reaches 72 % for $\Phi = 1.00$ and is 3.5 times higher than the corresponding mildly reacting fluid. For mixtures with $\Phi \geq 0.60$, the chemically active fluid states extend spatially beyond one integral length scale due to dilatation.

The above findings motivated a statistical analysis of fluid state interfaces encountered by traversing through the quinary multi-fluid field along the burner axis. The analysis provides insights into the multi-fluid structure and highlights the need for thermal support for low Da flows. The diagrams in Fig. 15 illustrate the multi-fluid interface probabilities for $\Phi = 0.2, 0.6$ and 1.0 . For $\Phi = 0.2$ the mixing fluid is primarily (98 %) adjacent to the reactant fluid. A distinct change of the fluid states adjacent to the reactants is evident for $\Phi = 1.0$ ($Da_1 = 5.1$) with the mixing fluid reduced from 98 % to 16 % in favour of the mildly reacting (6 %), strongly reacting (42 %) and product (36 %) fluids. The detachment of the mildly reacting fluid from the reactants by mixing and/or product fluid interlayers indicates the need for thermal support to initialise OH producing chemical activity for $Da_1 \leq 1.0$. The balance of fluid states sharing an interface with the mildly reacting fluid is strongly dependent on the Da_1 number as shown in Table 6.

The observed rates of strain, discussed below, prevent self-sustained burning for the leaner mixtures and thus the strongly reacting fluid is only defined for $\Phi \geq 0.6$ ($Da_1 \geq 1.0$). The probability of the strongly reacting fluid being adjacent to reactants decreases from 42 % for $\Phi = 1.0$ ($Da_1 = 5.1$) to 3 % for $\Phi = 0.6$ ($Da_1 = 1.2$) as also shown in Table 6 by means of interface probabilities. The interface of the mixing and strongly reacting fluid shows the reversed trend and dominates in the transitional case with $Da_1 \simeq 1.0$. The residual strongly reacting fluid shares interfaces with the mildly reacting or product fluids.

3.2 Unconditional Velocity Statistics

The unconditional velocity statistics along the stagnation point streamline, i.e. normalised mean axial (\bar{U}/U_b) velocity and its fluctuations, show the impact of the combustion heat release on the turbulent flow field (see Fig. 16). The location of the UN (LN) is at $X/D = 0.50$ (-0.50). In the proximity of the UN exit ($X/D > 0.2$) the \bar{U}/U_b ratio is not affected by the mixture reactivity as shown in the top row of Fig. 16. The impact of combustion on \bar{U}/U_b becomes evident at $X/D \leq 0.2$ by an eased and lagged deceleration of the mean flow with increasing Φ . This is caused by an earlier onset of chemical reaction and a more pronounced flow acceleration with increased heat release.

The axial and radial fluctuations ($\sqrt{u'u'}/U_b$ and $\sqrt{v'v'}/U_b$) are depicted in the middle and bottom row of Fig. 16. At $X/D > 0.2$ both components are independent of the mixture reactivity. Further downstream ($X/D < 0.2$) the velocity fluctuations are reduced with increasing mixture reactivity with the peak shifted towards the LN. A double peak of $\sqrt{u'u'}/U_b$ emerges at $\Phi \geq 0.80$, see middle row of Fig. 16, which is not observed at lower reactivities. The spatial location of the peak closer to the UN corresponds to the mean reaction onset. The second peak indicates the location of the mean interaction of the opposing streams. The strong dilatation effects and associated flow acceleration, pushes the stagnation plane towards the LN as evident in Fig. 16 (top and middle row). Similar trends were observed by Goh et al. [8, 33] at lower turbulence levels. The data show that the combustion mode transition is sufficiently strong to directly impact the flow field.

The velocity field along the upper nozzle exit, required for boundary conditions of computational studies, was provided by Hampp [22].

$$\begin{aligned}
 \overline{U_{k,FS,i,j}} &= \frac{1}{N} \sum_{n=1}^N c_{FS,n,i,j} \cdot U_{k,n,i,j} \quad \forall i, j \\
 (u'u')_{k,FS,i,j} &= \frac{1}{N} \sum_{n=1}^N c_{FS,n,i,j} \cdot (U_{k,n,i,j} - \overline{U_{k,FS,i,j}})^2 \quad \forall i, j \\
 C_{FS,i,j} &= \frac{1}{N} \sum_{n=1}^N c_{FS,n,i,j} \quad \forall i, j
 \end{aligned} \tag{5}$$

3.3 Conditional Velocity Statistics

Conditional velocity statistics allow the delineation of the interactions of each fluid state with the turbulent flow field as well providing a link to established bimodal segregation techniques, e.g. [31, 32, 46, 47, 51]. The multi-fluid classification permits conditioning for each fluid state, as shown in Eq. (5), and thus allows the quantification of the contribu-

tion of each individual (intermediate) fluid state. In Eq. (5), k is the axial or radial velocity component, n the instantaneous image, N the total number of images (i.e. 3000) and i and j the index variables. The instantaneous conditioning variable ($c_{FS,n}$) is defined as unity within the individual fluid state and nil elsewhere. The resulting fluid state progress variable (C_{FS}) is compiled identical to a conventional bimodal reaction progress variable [21] and, consequently, the criteria $\sum_{FS} C_{FS} = 1$ is maintained. The discussion is based on the aligned profiles and the data in physical space are included to ease the validation of numerical models. A minimum of 75 vectors was used for the determination of conditional velocities.

3.3.1 Conditional Reactant Fluid Velocity

The conditional mean axial reactant velocity ($\overline{U_r}/U_b$) and its axial ($\sqrt{(u'u')_r}/U_b$) and radial ($\sqrt{(v'v')_r}/U_b$) fluctuations are shown in Fig. 17. The stronger compression of the mean axial flow with increasing Da_1 due to the advanced reaction onset and elevated heat release, observed in Fig. 16, remains (see top row). The conditional reactant fluid velocity fluctuations (see middle and bottom rows) show a significant increase with decreasing Φ due to the shift of the reaction onset towards the stagnation plane and thus growing impact of the opposing stream.

3.3.2 Conditional Mixing Fluid Velocity

The mixing fluid probability distribution (Fig. 14b) has highlighted the importance of this fluid state, in particular for combustion processes with $Da_1 \leq 1.0$. The conditional mean axial mixing fluid velocity $\overline{U_{mix}}/U_b$ and turbulent fluctuations ($\sqrt{(u'u')_{mix}}/U_b$, $\sqrt{(v'v')_{mix}}/U_b$) are depicted in Fig. 18. The mixing velocities are significantly higher than the reactant velocities (compare to Fig. 17) for $Da_1 \leq 1$, which suggests HCP addition leading to increased momentum in the direction towards the UN. For flows with $Da_1 > 1.0$, a distinct drop in $\overline{U_{mix}}/U_b$ to the level of $\overline{U_r}/U_b$ is evident. Thus, the mixing fluid is aligned with the reactant flow field for $\Phi = 1.0$, indicating that only small HCP quantities are blended with the reactant fluid prior combustion.

At low Da_1 , the reactants accommodate more heat addition (HCP blending) while the turbulence intensity suppresses the immediate onset of OH producing chemical reactions. Hence, increased amounts of combustion products that alter or govern the mixing fluid flow dynamics lead to a gradual alignment of $\overline{U_{mix}}/U_b$ with the HCP fluid flow direction. This highlights the increasing need for thermal support to initialise the oxidation process for flows with $Da_1 \leq 1.0$ and suggests a gradual combustion regime transition away from self-sustained (e.g. corrugated flamelet) burning towards a supported distributed mode.

The corresponding axial ($\sqrt{(u'u')_{mix}}/U_b$) and radial ($\sqrt{(v'v')_{mix}}/U_b$) fluctuations (see middle and bottom rows) show a reduction in turbulent fluctuations with increasing Φ .

3.3.3 Conditional Mildly Reacting Fluid Velocity

Results obtained using velocity conditioning on the mildly reacting fluid, i.e. chemically active regions with reduced OH signal intensity, are shown in Fig. 19. Similarly to the mixing fluid, the conditional mean axial velocity (top row) reveals an increasingly HCP disturbed/driven flow with decreasing Da_1 . The impact is illustrated by the wide separation and increasingly positive $\overline{U_{mild}}/U_b$. The mixture with $\Phi = 1.0$ leads to negative $\overline{U_{mild}}/U_b$ close to the UN, i.e. is in line with the reactant flow. This implies that chemically active regions arise with little thermal support from the HCP stream. For leaner mixtures increasing HCP addition disturbs/drives the flow with $\overline{U_{mild}}/U_b$ becoming quickly positive and directed towards the UN.

The conditional velocity fluctuations are shown in the middle and bottom rows of Fig. 19. The axial component ($\sqrt{(u'u')_{mild}}/U_b$) shows a distinctly decreasing trend with increasing Φ and exhibits a more moderate slope with increasing reactivity that can be attributed to dilatation. The radial fluctuations show no distinct trend. The observations highlight the reduced influence of HCP addition with increasing mixture reactivity.

3.3.4 Conditional Strongly Reacting Fluid Velocity

The conditional strongly reacting fluid velocity and turbulent fluctuations, see Fig. 20, were evaluated for $Da_1 \geq 1.0$ (i.e. $\Phi = 0.60$ and 1.0). A clear flow acceleration towards the stagnation plane of $\overline{U_{str}}/U_b$ is observed, i.e. more negative values compared to $\overline{U_{mild}}/U_b$, due to the enhance dilatation. While the mildly reacting fluid velocity was governed by the HCP stream at $X/D < 0$, the strongly reacting fluid velocity of the stoichiometric case is aligned with the reactant flow direction (i.e. negative velocities). The conditional axial fluctuations of the strongly reacting fluid, see middle row of Fig. 20, are distinctly reduced for $Da_1 > 1.0$ as a consequence of the stronger heat release. Cases with $Da_1 > 1$ further exhibit slightly lower velocity fluctuations in the strongly reacting fluid than in the corresponding mildly reacting fluid, suggesting an increasingly dilatation driven flow.

3.3.5 Conditional Strain Distribution on Material Surfaces

The velocity gradients were conditioned upon the fluid state material surfaces (β). The strain rate ($e_{ij} = 0.5(\partial u_i/\partial x_j + \partial u_j/\partial x_i)$) and vorticity ($\omega_{ij} = \partial u_i/\partial x_j - \partial u_j/\partial x_i$) tensors were determined from the instantaneous planar PIV fields and subsequently conditioned upon β : $e_{\beta,ij} = e_{ij}|\beta$ and $\omega_{\beta,ij} = \omega_{ij}|\beta$, where $\beta \equiv 1$ at the iso-contour trajectory

and nil elsewhere. The tangent to the iso-contour was estimated at all positions (ζ) by a 3^{rd} order polynomial that was evaluated in the range of ± 16 pixels along β (twice the vector spacing). The strain rate tensor was rotated by the angle $\Theta (= \pi/2 - \theta)$ via $f_\beta = \mathbf{R} \cdot e_\beta$, where \mathbf{R} is the rotation matrix and θ is the angle between the tangential on $\beta|\zeta$ and the SPS. The normal (a_n) and tangential (a_t) strain rate components as well as the total strain (a_d) are defined in Eq. (6).

$$\begin{aligned} a_n &= f_{\beta,11} \\ a_t &= f_{\beta,22} \\ a_d &= e_{\beta,11} + e_{\beta,22} \end{aligned} \tag{6}$$

Results presented here include the movement of the stagnation point [10] with an applied radial limit of $\pm 0.5 L_I$ away from the stagnation point streamline. A more detailed discussion has been presented by Hampp and Lindstedt [24].

3.3.6 Strain Distribution along the Reactant Fluid Surface

The probability density function (PDF) of the a_n along the reactant fluid surface, depicted in Fig. 21, decreases progressively from mean compressive values found in the stagnation plane proximity (-1550 s^{-1}) for $\text{Da}_1 < 1.0$ to below the bulk strain rate based on the nozzle separation (-440 s^{-1}) for $\text{Da}_1 = 5.1$. The $\text{PDF}(a_n)$ is skewed towards extensive strains with its mode shifted from -1680 to -330 s^{-1} with increasing Φ . This can be attributed to the rapid transition to chemically active fluids states and a reaction onset shifted away from the stagnation plane. The augmented detachment with increasing Da_1 causes a modest reduction of the mean tangential component ($950 < a_t < 690 \text{ s}^{-1}$) with a distinctly squeezed PDF spread (i.e. rms reduced by $\sim 30 \%$) and reversed mode shift ($550 - 690 \text{ s}^{-1}$). The zero crossings, elevated skewness and reduced spread of the $\text{PDF}(a_n)$ and $\text{PDF}(a_t)$ with increasing Da_1 has been observed in experiments [52] and DNS [53]. The dilatation driven flow acceleration for $\text{Da}_1 > 1.0$ is highlighted by the total rate of strain shown in Fig. 21 (bottom left) with a shift from negative to positive mean values ($-750 < a_d < 310 \text{ s}^{-1}$). The earlier reaction onset further results in a reduced mean vorticity of the order of 50% for $\text{Da}_1 = 5.1$ compared to $\text{Da}_1 < 1.0$ (bottom right of Fig. 21). The mixing fluid is found primarily adjacent to the reactant fluid with qualitatively the same strain rate trends.

3.3.7 Strain Distribution along Chemically Active Fluid Surfaces

For $\text{Da}_1 \leq 1.0$, the mildly reacting fluid was spatially separated ($> 90 \%$) from the reactant fluid by a mixing and/or product fluid interlayer that suggests a need for thermal support.

The strong impact of the HCP on the mildly reacting fluid surface results in a Da_1 independent $a_n \simeq -1340 \text{ s}^{-1}$, see Fig. 22. The determined a_n is well beyond the extinction strain rate for the transitional case with $Da_1 \simeq 1.0$ ($a_q = 600 \text{ s}^{-1}$). The tails of the $PDF(a_n)$ also exceed the extinction point for mixtures with $Da_1 = 5.1$ ($a_q = 3100 \text{ s}^{-1}$). The lack of flow alignment for low Da_1 flows was also found by Chakraborty and Swaminathan [53] at $Re_t \simeq 50$. The turbulent mixing driven flow and thermal HCP support for the mildly reacting fluid results in vorticity levels found in the proximity of the stagnation plane that are independent of Da_1 .

The transition to strongly exothermic fluid states collocates the flow acceleration normal to the flame front and results in a compressive strain reduction from -1050 to -660 s^{-1} , i.e. around a 40 % reduction for $\Phi = 1.0$ ($Da_1 = 5.1$) compared to $\Phi = 0.6$ ($Da_1 = 1.2$), as depicted in Fig. 23. This further corresponds to a decrease of 50 % compared to the MR surface for $\Phi = 1.0$. The tangential acceleration caused by combustion results in increased extensive strain ($650 < a_t < 830 \text{ s}^{-1}$). The shift of the $PDF(a_n)$ towards reduced normal strain with a similar mean, but reduced spread of the $PDF(a_t)$ coupled with a more pronounced skewness with increasing Da_1 , was qualitatively also shown in DNS data by Chakraborty and Swaminathan [53]. A transition from contracting to dilating a_d (-400 to 160 s^{-1}) is evident for high Da_1 as shown in the bottom left of Fig. 23. The preferential alignment of the flame front normal perpendicular to the extensive strain [54] becomes evident at high Da_1 due to the favoured stabilisation of self-sustained flames in low compressive strain regions ($a_n < a_q$) that are detached from the stagnation plane. The reduction in turbulent flame speed for lower Da_1 [32] leads to a flame anchoring in the proximity of the stagnation plane with elevated normal strain levels and attenuated dilatation [55]. The more ordered flow field with increasing Da_1 is also reflected by a significant vorticity mitigation (bottom right in Fig. 23) of the order of 25 % for $\Phi = 1.0$ ($Da_1 = 5.1$) compared to $\Phi = 0.6$ ($Da_1 = 1.2$). This also corresponds to a ~ 40 % reduction of the mean strongly reacting fluid vorticity compared to the mildly reacting value for $\Phi = 1.0$.

3.4 Bimodal Flow Analysis

Bimodal velocity statistics are frequently inferred from PIV particle density segregation techniques (DST) [46] or based on the OH-PLIF signal [56]. Hampp and Lindstedt [24] applied a PIV based segregation technique to delineate the current data series. A distinctly reduced gradient transport was shown with increasing Φ , yet the transition to counter-gradient transport was suppressed even for the stoichiometric flame. The accuracy of two-fluid descriptions can be evaluated by comparing the PIV and OH-PLIF based techniques and computing the differences (Δ) of the conditional reactant ($\Delta\overline{U_r}$), product ($\Delta\overline{U_p}$) and

slip ($\Delta \overline{U}_s$) velocities and the scalar flux ($\Delta(\overline{cu})$) as shown in Fig. 24. At high Da , the definitions show good agreement as only thin interfaces separate reactants from OH rich combustion products. At $Da \leq 1$ substantial discrepancies emerge as the Mie scattering iso-contour detaches from the OH producing chemically active zones due to the need for thermal support.

3.5 Impact of Excess Enthalpy on the Burning Mode Transition

The analysis above has shown that the HCP exerts a distinct impact on the burning mode and thus the impact of the excess enthalpy is investigated. Local flame quenching in the BTB configuration is primarily caused by the high strain acting on the flame front. Re-ignition occurs either due to conventional flame propagation or by means of HCP support (e.g. resulting in auto-ignition). The impact of the HCP temperature is investigated for the case with $Da_1 \simeq 1.0$ (DME at $\Phi = 0.6$), which marks the approximate transition from thin flamelets to distributed reaction zones. The adiabatic flame temperature of the laminar, unstrained, flame is $T_{ad} = 1755$ K, but reduces quickly to 1555 K under extinction conditions ($a_q = 600 \text{ s}^{-1}$). The HCP temperature is varied in the range $1600 < T_{HCP} < 1800$ K, leading to super-adiabatic conditions with heat transfer from the HCP to the reaction zone. The lower limit corresponds approximately to the extinction temperature and the upper limit is just above the adiabatic flame temperature, i.e. $T_q < T_{HCP} \leq T_{ad}$. The ignition delay time was estimated to correspond to the integral time scale of turbulence at a temperature of 1200 K (see Section 3.6). For the current Re_t , HCP supported re-ignition is therefore assured.

3.5.1 Multi-Fluid Probability Statistics

The multi-fluid analysis has shown a clear redistribution of the fluid states with varying Da_1 . At low Da_1 , supported burning was favoured, while at high Da_1 self-sustained combustion was increasingly realised. The reactant fluid probability is essentially independent of the HCP enthalpy. The HCP impact becomes more evident for mixing fluid peak probability, see Fig. 25b. The probability is reduced away from the origin due to the promoted reaction onset and significantly reduced auto-ignition delay time from 17.6 to 5.1 μs with increasing T_{HCP} . This further result in a pronounced augmentation of the mildly reacting fluid from 13 – 35 % with increasing T_{HCP} as depicted in Fig. 25c.

Modest HCP blending fractions with insufficient enthalpy addition to initialise auto-ignition may cause elevated Da_1 and thus promote conventional burning. Coriton et al. [9] observed the extension of the intermittent and stable flame region towards higher product

temperatures for elevated a_b of premixed CH_4 flames. Although the unstable regime is not observed for the DME/air flames for the current T_{HCP} range and Re_t , a change in burning mode under super-adiabatic conditions is prominent. The augmentation of conventional burning is illustrated by means of the strongly reacting fluid probability in Fig. 25d, which increases from 2 % for $T_{HCP} = 1600$ K to approximately 30 % for $T_{HCP} = 1800$ K. The spatial extent of all fluid probabilities is essentially limited to one L_I for all T_{HCP} .

The interfaces encountered by traversing along the burner axis through the quinary multi-fluid field are shown in Table 7 for all cases investigated and visualised for $T_{HCP} = 1600$ and 1800 K in Fig. 26. In the instance of $T_{HCP} = 1800$ K, 46 % of the reactant fluid is observed adjacent to the mixing fluid, which corresponds to 20 % of all interfaces. The mildly and strongly reacting fluid is adjoining the reactant fluid with a likelihood of 13 and 19 %, respectively, which allocates 23 % to the product fluid. At a reduced T_{HCP} ($= 1600$ K), the neighbouring mixing fluid probability increases to 78 % with adjoining mildly and strongly reacting fluids reduced to 6 and 1 %, respectively, allocating 15 % to the product fluid.

The mildly reacting fluid is primarily (60 %) in the direct proximity of the product fluid and independent of T_{HCP} . For a high HCP enthalpy, the residual adjacent fluid is composed of 15 % reactant fluid, 16 % strongly reacting fluid and 8 % mixing fluid. The latter increases to 24 % for $T_{HCP} = 1600$ K at the expense of reduced adjacent reactant (11 %) and strongly reacting (5 %) fluids. The strongly reacting fluid is found primarily adjacent to the mixing (24 %) and product (45 %) fluid for the case $T_{HCP} = 1600$ K, but is evenly distributed (25 ± 3 %) across all fluid states for high HCP enthalpies. Consequently, the interface statistics suggest a shift towards elevated blending fraction for reduced HCP enthalpy streams in order to initialise the onset of OH producing chemical reactions.

3.5.2 Conditional Velocity Statistics

The subsequent analysis focuses on the intermediate cases with $T_{HCP} = 1650$, 1700 and 1750 K due to a modest disturbance of the stagnation plane by the LN HCP stream for the limiting conditions with $T_{HCP} = 1600$ and 1800 K. Such disturbances can be removed by optimising the HCP stream conditions for alternative temperature windows. Unconditional velocity statistics for the discussed conditions were presented by Hampp [22].

Multi-fluid conditional velocity statistics are used to delineate the influence of the HCP enthalpy on the burning mode transition. The data are evaluated along the burner axis and aligned at the Mie scattering iso-contour ($x_s = 0$). The conditional mean axial fluid state (FS) velocities ($\overline{U_{FS}}$) are normalised by the UN bulk velocity (U_b). The axial ($\overline{u'_{0,FS}}$) and radial ($\overline{v'_{0,FS}}$) velocity fluctuations are normalised by the respective reactant fluid velocity fluctuations, measured 1 mm away from the nozzle exit ($\overline{u'_{r,NE}}$, $\overline{v'_{r,NE}}$). The normalisation

eliminates modest discrepancies between the cases and provides a direct measure of the HCP enthalpy impact on the turbulent flow field.

The conditional reactant fluid velocity prior the reaction onset ($x_s < 0$) is, naturally for a flow with constant Da_1 and Re_t , not affected by the HCP enthalpy emerging the LN. The impact of the HCP enthalpy on the thermally altered fluid material becomes evident in the conditional mixing fluid velocity ($\overline{U_{0,mix}}/U_b$) through an increasingly HCP driven flow field for reduced T_{HCP} , see Fig. 27. For $T_{HCP} = 1750$ K, $\overline{U_{0,mix}}/U_b$ is negative in the direct proximity of the origin, i.e. in line with the reactant flow, while ≥ 0 for lower T_{HCP} . This can be attributed to the enhanced blending capacity by the premixed reactants prior the onset of OH producing chemical activity with reduced HCP enthalpy. The higher HCP blending quantities also cause elevated axial and radial mixing fluid fluctuations, with the latter being distinctly higher than the corresponding reactant fluid velocity fluctuations in a comparable spatial location.

In the proximity of the origin, the conditional mildly reacting fluid velocity ($\overline{U_{0,mild}}/U_b$) is independent of the HCP enthalpy as illustrated in Fig. 28. The impact becomes clear by the separation of $\overline{U_{0,mild}}/U_b$ far away from the origin ($x_s / L_I > 0.5$). The eased gradients for higher T_{HCP} are caused by a flow acceleration towards the stagnation plane due to a more pronounced dilatation. The latter can at least be attributed to reduced HCP dilution levels. The increasingly dilatation driven flowfield further yields a distinct reduction in axial and radial fluctuations. The $\sqrt{(u'u')_{mild}}/\sqrt{(u'u')_{r,NE}}$ show a modest reduction compared to the mixing fluid while the radial component exhibits elevated fluctuations. The conditional mean axial strongly reacting fluid velocity is, by contrast to the mildly reacting fluid velocity, insensitive to the HCP enthalpy. This is characteristic for a self-sustained burning at constant Da_1 and Re_t in the absence of HCP dilution.

3.5.3 Conditional Strain along Material Surfaces

The normal (a_n) and tangential (a_t) strain conditioned upon the reactant fluid iso-contour is depicted in Fig. 29 along with the corresponding total rate of strain (a_d) and vorticity (ω). To recapitulate, the LN HCP exerted a vanishing effect on the conditional reactant fluid velocities. The $a_n|R$, however, illustrate a modest shift of the PDF towards gradually reduced mean compressive values ($-1570 < a_n < -1250$ s⁻¹ for $1650 < T_{HCP} < 1750$ K). The slight detachment of the reactant fluid iso-contour from the stagnation plane with increasing HCP enthalpy further causes a reduced mean tangential ($1000 < a_t < 800$ s⁻¹) and total contracting ($-730 < a_d < -500$ s⁻¹) strain with reduced mean vorticity levels ($2810 < \omega < 2310$ s⁻¹). Moreover, the spread of all PDFs is reduced by ~ 10 % with increasing T_{HCP} suggesting a first thermal alteration that is increasingly caused by adjacent exothermic reactions. The velocity gradients conditioned upon the mixing ($a_n|M$, $a_t|M$,

$\omega|M)$ and mildly reacting fluid surfaces ($a_n|MR$, $a_t|MR$, $\omega|MR$) show similar trends with details reported by Hampp [22].

For $T_{HCP} = 1750$ K, the reaction onset of the strongly reacting fluid is anchored in comparatively low compressive strain regions with a mean of $a_n = -920 \text{ s}^{-1}$ compared to $a_n = -1250 \text{ s}^{-1}$ for $T_{HCP} = 1650$ K. The $\text{PDF}(a_n|SR)$ at $T_{HCP} = 1750$ K further shows a distinctly elevated skewness towards decreased compressive strain compared to lower HCP enthalpies as well as to fluid states with reduced reactivity. A significant vorticity attenuation of 25 % is observed for $T_{HCP} = 1750$ K compared to 1650 K and up to 15 % compared to the reactant fluid surface.

3.6 Combustion Regime Transitions

The estimated combustion modes based on Da_1 are shown in Fig. 30 using a Borghi diagram and are listed, along with dissipation rates, Kolmogorov length and timescales and Ka_1 in Table 2. The dissipation rate within the reactants was also used to estimate a total (mean) rate of strain (a_T) via the relationship of Kostiuk et al. [57]:

$$a_T = a_b + a_I = 2 \cdot \frac{U_b}{H} + \left(\frac{\varepsilon_r}{\nu_r} \right)^{1/2} \quad (7)$$

The bulk $a_b \approx 750 \text{ s}^{-1}$ and turbulent strain $a_I \approx 3200 \text{ s}^{-1}$ lead to $a_T \approx 3950 \text{ s}^{-1}$ ($> a_q$ for $\Phi = 1.0$) within the reactants (see Table 2). The rate of strain analysis along the material surfaces, see Section 3.3.5, has illustrated the burning of conventional flames in low strain regions with the need of thermal HCP support to sustain combustion beyond the conventional (strained twin flame) extinction limit, which exerts some influence for all mixtures.

The blending of HCP with the reactant fluid will raise the temperature and the resulting mixture may auto-ignite depending on the delay time. A second Damköhler number can be used to delineate the transition from conventional flame propagation to an auto-ignition mode. Accordingly, auto-ignition delay times were computed for relevant initial temperatures (1000 – 1700 K) and equivalence ratios ($\Phi = 0.20, 0.60$ and 1.0) as shown in Fig. 7. The auto-ignition Damköhler number (Da_2) is here related to the degree of mixing inside a gas pocket as shown in Eq. (8).

$$\text{Da}_2 = \frac{\tau_I}{\tau_{ign}} \quad (8)$$

The exponential temperature dependency of τ_{ign} suggests that ignition will occur close to the peak temperature within a fluid pocket. Consequently, the expected range is bounded by the HCP temperature of 1700 K ($\text{Da}_2 = 214$; $\tau_{ign} = 12.6 \mu\text{s}$) and the temperature

(≈ 1196 K; $\tau_{ign} = 2.5$ ms) giving $Da_2 = 1$. A corresponding auto-ignition Karlovitz number can readily be defined.

$$Ka_2 = \frac{\tau_{ign}}{\tau_\eta} \quad (9)$$

The auto-ignition process also depends on the bulk flow motion and a third Damköhler number (Da_3), see Eq. (10), was defined based on a convection residence time τ_b ($\simeq 8.7$ ms). The latter was estimated by following the mean trajectory of a fluid parcel along the stagnation point streamline from the onset of reaction/mixing using a reaction progress variable iso-contour of $\bar{c} = 0.02$ [32, 58] until it is convected radially out of the domain (i.e. $y = \pm 0.015$ m).

$$Da_3 = \frac{\tau_b}{\tau_{ign}} \quad (10)$$

The auto-ignition Damköhler numbers (Da_2 and Da_3) and the corresponding Karlovitz number (Ka_2) were used to derive the auto-ignition regime diagram shown in Fig. 31. On the right hand side of the Da_3 line, unreacted mixture is likely to be convected out of the domain without ignition (assuming the absence of conventional flame propagation). Left of the $1/Ka_2$ line, the mixture is auto-igniting on a timescale shorter than the Kolmogorov timescale. The Da_3 and $1/Ka_2$ consequently bound the auto-ignition manifold for present study. The initial temperature (T_0) axis of this diagram can be considered a third dimension of a revised combustion regime diagram (see Figs. 30 and 31) which intersects at a given Re_t and temperature. The conventional Da_1 numbers can readily be added to Fig. 31 at $T_0 = 320$ K. Further, the impact of a Φ variation on Da_2 is comparatively modest for DME. Under the current conditions (e.g. $Da_3 > 700$ and $Ka_2 \approx 0.05$) any residual reactants will auto-ignite in the hot combustion products. It is estimated that DME combustion in an auto-ignition mode can be sustained down to temperatures around 1200 K at the current Re_t . Further, no intermittent (pulsating) regime was observed. By contrast, pulsating auto-ignition events have been observed for CH_4 /air at approximately $\Phi = 0.7$ and $T_{HCP} = 1700$ K, similar to the observations by Coriton et al. [9].

The characteristic values for the T_{HCP} variation are listed in Table 4. The conventional Da_1 is maintained constant at ~ 1.1 with a constant at $Re_t \simeq 395$ and fine scale Karlovitz number ($Ka_1 \simeq 7.0$). The auto-ignition delay time (τ_{ign}) decreases from 17.6 to 5.1 μ s within the T_{HCP} range from 1600 to 1800 K, which results in a threefold reduction of the auto-ignition Damköhler number ($140 < Da_2 < 500$). The resulting auto-ignition Ka_2 increases gradually from 0.015 to 0.057 with decreasing HCP enthalpy. The results indicate an impact on the burning mode due to the reduced auto-ignition delay time for elevated HCP enthalpies. With increased T_{HCP} , the thermochemical conversion shifts away from a

strong HCP dilution towards progressively self-sustained burning that is possibly initialised by small HCP blending fractions.

3.7 Calculation Methods for Distributed Combustion Regimes

The application of calculation methods that do not rely on presumed (e.g. topological or flamelet) structures requires the introduction of multiple chemical time-scales. The inclusion of the latter into turbulent flowfield simulations is associated with exceptionally high computational costs. However, use of the transported probability density function (pdf) approach for the inclusion of the thermochemistry allows the development of highly efficient parallel algorithms for large stochastic systems. To this effect, the scope of parallelising the treatment of the chemistry in the context of transported joint-*pdf* methods has also been explored on different platforms in order to permit more effective computations featuring the direct implementation of extended mechanisms for practical fuels. The latter are of a size approaching that of mechanisms based on the rapid decomposition hypothesis leading to the C_1 – C_2 and/or C_1 – C_4 foundation chemistry [26]. The work outlined therefore forms a step towards establishing if mechanisms of the latter type can reproduce measured trends associated with combustion regime transitions.

The Lagrangian nature of stochastic particle calculations, typically used in the solution method for the transported joint-*pdf*, potentially permits an efficient parallelisation. The most computational demanding part of the elliptic calculations is the associated Monte Carlo part used for the calculation of the chemical source term. Apart from the molecular mixing model, the rest of the method for each stochastic particle can be calculated individually, which allows high efficiency. In addition, a high number of particles of unmixed fuel or oxidiser are non-reactive and thus have a minimal computational cost, which leads to the requirement of fine tuning the load balancing among the processes. In terms of performance cost, inter-communications at the beginning of each Monte Carlo step have to take place in order to distribute the particles among the processes. At the end of the Monte Carlo step, an operation also has to take place to calculate the global statistics. Mixing models form part of the calculation method and may be considered local or non-local. In the case of non-local models, the interacting particles are chosen randomly from the composition space, while in case of the local models the particles should mix with other particles in their immediate neighbourhood in composition space. Therefore, depending on the localness of the mixing model and the implementation of the data/particle parallelisation (i.e. how the data/particles are stored among the processes), this might lead into further complications (e.g. extra inter-process communications).

Amdahl's Law [64] can be used to calculate the theoretical maximum speed-up ob-

tained by using parallel processes as compared to serial execution. The speed-up can be defined as a relative change (or efficiency), with a potential maximum value of 1 (100 %), A code can be separated into two parts, the part which can be parallelised and the part which cannot (or will not) be parallelised. Let the parallelised part consume a fraction "p" of the total initial wall time. Additionally, let "s" be the reduction in latency of the parallelised part, which in this case is the total number of processes. Then, the theoretical speed-up in term of wall time is S_1 or as a relative change S_2 .

$$S_1(s) = \frac{1}{1 - p - \frac{p}{s}} \quad (11)$$

$$S_2(s) = p \left(1 - \frac{1}{s} \right) \quad (12)$$

Figure 32 presents graphically the theoretical maximum speed-up as a relative change (Eq. 12) if the parallelised part of the code accounts for 50 %, 75 %, 95 %, and 99 % of the initial wall time. However, this analysis does not take into account various factors which might lead into increased latency. For example, using a distributed-memory communication implementation, such as MPI, implies additional delays.

Both MPI and GPGPU implementations constitute Multiple Data Stream Models [65]. Therefore, how data is stored in memory is significant for their communications. Generally, there are two distinct ways of storing the data: Structure of Arrays (SoA) and Array of Structures (AoS). Figure 33 presents three actual code arrays OMP, WTP, and PAR of size 250,000 stored in a SoA on the left and in an AoS on the right. In FORTRAN 77, array sizes are predefined at compilation time, therefore there is a tendency to define significantly bigger arrays than the necessary. Thus, in blue colour, up to element 24,000 (arbitrarily chosen as an example) are the elements in use, while, in orange colour, from element 24,000 until the end are noted as unused elements. The two implementations have several trade-offs. A SoA could potentially be more effective since grouping together the same database could lead into vectorisation. An AoS offers memory read/write coalescing (all data of an object accessed at the same time). However, if multiple processes trying to access the same data simultaneously, then this might lead into extra latency. Considering the data communications, the AoS allows the bundling of all arrays into one inter-communication for each process without sending the unused elements of the arrays, the elements 24,001 to 250,000 in Fig. 33. In the current work, the simulation code was rewritten in AoS. The serial code featuring SoA was roughly 1.5% slower. However, after its implementation on the parallel MPI code, the AoS structure significantly reduced the MPI communications latency, improving remarkably the overall efficiency as discussed below.

3.7.1 Efficiency Gains from Parallelisation

The current evaluation configuration uses a Cabra burner geometry [66, 67] that permits detailed studies of turbulence-chemistry interactions. The configuration is of particular relevance to auto-ignition dominated flows of the kind that can be expected to exert increasing influence for distributed combustion modes. Several studies have been performed for this geometry (e.g. [68, 71]) using methane as fuel. In addition H_2 flames have been studied and simulated using transported-*pdf* based methods [66, 69]. A wide range of mixing models and chemical kinetic mechanisms have also been used with a good agreement between computational and experimental results, which suggests that the flames are controlled by chemical kinetics. There are, accordingly, good reasons to use this configuration. Results obtained with detailed methane chemistry [71], featuring 44 species and 256 reactions, as well as a much smaller hydrogen mechanism featuring 9 species and 19 chemical reactions, are presented below.

The serial code version of PIPER ([71]) was used as a test bed. Computer science evolves rapidly and there have been many changes regarding the Operating Systems (OS), the compilers and their libraries. The stochastic nature of the solution method makes it potentially sensitive to such changes. An interesting example is the case of extended precision, when a single-precision constant is assigned to a double-precision variable. It used to be evaluated as double precision according to FORTRAN 77 Standards. However, according to Fortran 90/95 Standard rules, it is now evaluated as single precision, which essentially means that the rest of the digits are random. In order to allow compatibility with FORTRAN 77 Standards, all constant assignments have to be explicitly defined with double precision accuracy, or, in case of Intel compiler, the flag `-fpconstant` can be used. The current testing was performed predominantly on the Imperial College HCP cluster operating under Oracle Server 6.7. However, other OS (OS X 10.11, Windows 8.1 and CentOS 7) were also evaluated with similar outcomes.

The results from the parallelised code show, as expected, no significant differences in results as can be seen in Fig. 34, which compares the maximum OH concentrations of the serial and the MPI versions of PIPER using the detailed mechanisms for H_2 and CH_4 . The differences between the results are insignificant and can be attributed to the different Random Number Generators (RNGs). The benefits of parallelisation can be seen in Fig. 35, which presents the achieved speed-up with each bar representing the normalised wall time. The run time was hence reduced down to 4.5 minutes from 27 minutes in case of H_2 and down to 80 minutes from nearly 9 hours in case of CH_4 . The difference between the theoretical maximum speed and that achieved is less than 10% for both cases. The limitations on the number of processes used is due to the comparatively small physical

domains chosen (ie. computational cells). Overall, it is clear that close to the theoretical maximum speed-up can be achieved. Accordingly, it can be expected that methods of the current type can be combined directly with mechanisms based on the rapid decomposition hypothesis leading to the C_1 – C_2 and/or C_1 – C_4 foundation chemistry [26] to compute the current compact experimental domains.

4 Conclusions

Combustion regime transitions from close to the corrugated flamelet regime to distributed reaction zones were systematically investigated with examples given for lean premixed DM/air flames under turbulent conditions ($Re_t \simeq 380$). An opposed jet back-to-burnt configuration with fractal grid generated turbulence was used with a temperature controlled burnt gas state. The chemical timescale was varied by means of the upper nozzle equivalence ratio ($0.2 \leq \Phi_{UN} \leq 1.0$) resulting in an estimated Damköhler number (Da_1) range of $0.06 \leq Da_1 \leq 5.2$. The stabilising hot combustion products (HCP) emerging from the lower nozzle were created using stoichiometric H_2 flames with the temperature controlled by means of CO_2 dilution in the range $1600 < T_{HCP} < 1800$ K.

The multi-fluid concept of Spalding [25] was explored by means of simultaneous Mie scattering, OH-PLIF and PIV. The multi-fluid analysis has the potential to extend methods based on bimodal approximations, such as the BML [21] framework, by permitting intermediate fluid states, which is of particular importance for low Da_1 flows. Five fluid states were selected in the present work and thermochemical interpretations provided: reactants, combustion products, mixing fluids, mildly and strongly reacting (flamelet-like) fluids.

The combustion regime transition from self-sustained flame propagation towards a distributed/supported burning mode was quantified using the multi-fluid analysis with a gradual, but distinct, redistribution between the defined fluid states observed with decreasing Da_1 . The interface and adjacent fluid state statistics provided further insight of the observed fluid state reallocation. The fluid state that represents self-sustained burning was observed with a 40 % probability directly adjacent to the reactant fluid for $\Phi = 1.0$ ($Da_1 = 5.1$), which was significantly reduced with Da_1 in favour of interlayers of reduced reactivity. The less reactive fluid states were increasingly separated from the reactants by a layer acting as an enthalpy source. This resulted in a mildly reacting fluid peak probability that was shifted towards the stagnation plane.

The current work further showed a distinct fluid acceleration due to increased heat release at high Da_1 , while the flow field was dominated by the hot combustion product blending for less reactive mixtures. The multi-fluid delineation of the combustion process hence allowed the separation of the contributions made by the various fluid states. The

proximity of the stagnation plane was characterised by a high compressive axial strain that increasingly prevented self-sustained burning for reduced Damköhler numbers. The increasing influence of hot combustion product support resulted in highly strained and Da_1 independent chemically active zones with no favoured dilatation direction – consistent with an auto-ignition related burning mode. By contrast, a preferential alignment of the flame front normal with the principal extensive strain and significantly reduced vorticity levels were evident for self-sustained flames with high Da_1 . The associated dilatation caused a reduction of the gradient scalar flux. However, the transition to counter-gradient scalar transport was suppressed under the current conditions ($Re_t \simeq 380$).

The multi-fluid analysis was further used to delineate the impact of the HCP enthalpy on the burning mode transition. The DME case marking the estimated transition from the thin reaction zone to distributed burning (i.e. $\Phi = 0.6$) was stabilised against HCP streams of varying temperature ($1600 < T_{HCP} < 1800$ K). The multi-fluid probability and interface statistics illustrated the advanced initialisation of chemically active fluid states with reduced blending fractions for higher T_{HCP} . A substantial augmentation of the strongly reacting fluid was observed for T_{HCP} in excess of the adiabatic flame temperature. By contrast, the strongly reacting fluid nearly vanished for T_{HCP} of the order of the extinction temperature. The absence/reduction of HCP diluents in the chemically active fluids caused a transition away from distributed towards self-sustained burning with increasing HCP enthalpy. The turbulence – chemistry interaction was evaluated in the range $1650 < T_{HCP} < 1750$ K. Despite the narrow variation, the exponential temperature dependency of the auto-ignition process resulted in clear trends and highlighted an incrementally stronger and directed dilatation with increasing HCP enthalpy that was attributed to reduced blending fractions. By contrast, the velocity statistics of the strongly reacting fluid, representing a fluid state with little or no HCP support, was not affected by the HCP enthalpy. The strain distribution along the multi-fluid material surfaces indicated a gradual detachment of the reaction onset from the stagnation plane with increasing HCP enthalpy that was attributed to an eased reaction onset at lower HCP blending fractions.

The results of all cases were further evaluated in the context of conventional and auto-ignition based Damköhler and Karlovitz numbers and it was shown that the failure to establish conventional turbulent flames leads to a combustion mode that is dominated by the hot combustion product temperature. With increasing HCP enthalpy, self-sustained burning was promoted due to an eased reaction onset. The classification of the data in a conventional Borghi diagram showed the wide distribution with varying equivalence ratio, while the auto-ignition dimensions advanced the fundamental understanding of the observed differences of the turbulence-chemistry interaction between the investigated fuels.

The current work has illustrated the need for a more comprehensive analysis technique

for combustion processes with low Damköhler and high turbulent Reynolds number. The current multi-fluid delineation removes the assumption of thin reaction zones and has provided novel insight into combustion regime transitions. The analysis further highlighted the distinct need to accurately model the combustion chemistry – in particular for low Da_1 flows. The obtained data are expected to be particularly useful for the evaluation of models that do not assume a flame front structure and may thus be used to characterise burning mode transitions. It has been shown that such models can be efficiently parallelised with a performance close to the theoretical maximum.

5 Acknowledgements

The authors would like to acknowledge the support of the ONR under Grant N62909-12-1-7127 and AFOSR and EOARD under Grant FA8655-13-1-3024. The authors wish to thank Dr Gabriel Roy, Dr Chiping Li, Dr Gregg Abate and Dr Russ Cummings for encouraging the work.

6 References

- [1] T. Plessing, N. Peters, J. G. Wüning, Laseroptical investigation of highly preheated combustion with strong exhaust gas recirculation, *Proc. Combust. Inst.* 27 (2) (1998) pp. 3197–3204.
- [2] J. Wüning, J. Wüning, Flameless oxidation to reduce thermal NO-formation, *Prog. Energ. Combust.* 23 (1) (1997) pp. 81–94.
- [3] M. Katsuki, T. Hasegawa, The science and technology of combustion in highly preheated air, *Proc. Combust. Inst.* 27 (1998) pp. 3135–3146.
- [4] B. B. Dally, A. N. Karpetis, R. S. Barlow, Structure of turbulent non-premixed jet flames in a diluted hot coflow, *Proc. Combust. Inst.* 29 (2002) pp. 1147–1154.
- [5] A. Parente, J. C. Sutherland, B. B. Dally, L. Tognotti, P. J. Smith, Investigation of the MILD combustion regime via principal component analysis, *Proc. Combust. Inst.* 33 (2011) pp. 3333–3341.
- [6] E. Mastorakos, A. Taylor, J. Whitelaw, Extinction of Turbulent Counterflow Flames with Reactants Diluted by Hot Products, *Combust. Flame* 102 (1995) pp. 101–114.
- [7] P. Geipel, K. H. H. Goh, R. P. Lindstedt, The stability of flames burning against hot exhaust products in fractal generated turbulence, *Proc. ECM*, 2011.
- [8] K. H. H. Goh, P. Geipel, F. Hampf, R. P. Lindstedt, Regime transition from premixed to flameless oxidation in turbulent JP-10 flames, *Proc. Combust. Inst.* 34 (2013) pp. 3311–3318.

- [9] B. Coriton, J. H. Frank, A. Gomez, Effects of strain rate, turbulence, reactant stoichiometry and heat losses on the interaction of turbulent premixed flames with stoichiometric counterflowing combustion products, *Combust. Flame* 160 (2013) pp. 2442–2456.
- [10] P. Geipel, K. H. H. Goh, R. P. Lindstedt, Fractal-Generated Turbulence in Opposed Jet Flows, *Flow Turbul. Combust.* 85 (2010) pp. 397–419.
- [11] D. Geyer, A. Kempf, A. Dreizler, J. Janicka, Turbulent opposed-jet flames: A critical benchmark experiment for combustion LES, *Combust. Flame* 143 (2005) pp. 524–548.
- [12] S. C. Sorenson, S. E. Mikkelsen, Performance and emissions of a 0.273 liter direct injection diesel engine field with neat dimethyl ether, *SAE* (1995) 950064.
- [13] T. Fleisch, C. McCarthy, A. Basu, C. Udovich, P. Charbonneau, W. Slodowske, S.E Mikkelsen, J. McCandless, A new clean diesel technology: Demonstration of ULEV emissions on a navistar diesel engine fuelled with dimethyl ether, *SAE* (1995) pp. 950061.
- [14] C. Arcoumanis, C. Bae, R. Crookes, E. Kinoshita, The potential of di-methyl ether (DME) as an alternative fuel for compression-ignition engines: A review, *Fuel* 87 (2008) pp. 1014–1030.
- [15] P. Allison, Y. Chen, J. F. Driscoll, Investigation of Dimethyl Ether Combustion Instabilities in a Partially-Premixed Gas Turbine Model Combustor Using High-Speed Laser Diagnostics, *AIAA* 52 (2014), DOI: 10.2514/6.2014-0660.
- [16] C. A. Daly, J. M. Simmie, J. Wuermel, N. Djeballi, C. Paillard, Burning velocities of dimethyl ether and air, *Combust. Flame* 125 (2001) pp. 1329–1340.
- [17] Z. Zhao, A. Kazakov, F.L. Dryer, Measurements of dimethyl ether/air mixture burning velocities by using particle image velocimetry, *Combust. Flame* 139 (2004) pp. 52–60.
- [18] Y. L. Wang, A. T. Holley, C. Ji, F. N. Egolfopoulos, T. T. Tsotsis, H. J. Curran, Propagation and extinction of premixed dimethyl-ether/air flames, *Proc. Combust. Inst.* 32 (2009) pp. 1035–1042.
- [19] F. Fuest, R. S. Barlow, J. Y. Chen, A. Dreizler, Raman/Rayleigh scattering and CO-LIF measurements in laminar and turbulent jet flames of dimethyl ether, *Combust. Flame* 159 (2012) pp. 2533–2562.

- [20] K. N. Gabet, H. Shen, R. A. Patton, F. Fuest, J. A. Sutton, A comparison of turbulent dimethyl ether and methane non-premixed flame structure, *Proc. Combust. Inst.* 34 (2013) pp. 1447–1454.
- [21] K. N. C. Bray, Laminar Flamelets and the Bray, Moss, and Libby Model, in N. Swaminathan, K. N. C. Bray (Eds.), *Turbulent Premixed Flames*, Cambridge University Press, 2011 pp. 41–60, ISBN: 978-0-521-76961-7.
- [22] F. Hampp, Quantification of Combustion Regime Transitions, PhD thesis, Imperial College, May 2016 url: <http://hdl.handle.net/10044/1/32582>
- [23] F. Hampp, R. P. Lindstedt, Fractal Grid Generated Turbulence - A Bridge to Practical Combustion Applications, in Y. Sakai and C. Vassilicos (eds.) *Fractal Flow Design: How to Design Bespoke Turbulence and why*, Springer-Verlag, CISM Int. Mech. Sci. 568, 2016, DOI:10.1007/978-3-319-33310-6 3.
- [24] F. Hampp, R. P. Lindstedt, Strain distribution on material surfaces during combustion regime transitions, *Proc. Combust. Inst.* (2016) Accepted for publication. <http://dx.doi.org/10.1016/j.proci.2016.07.018>
- [25] D.B. Spalding, Multi-fluid models of turbulent combustion, *Proc. Seventh Biennial Conf. on Comp. Techn. Applications (CTAC 95)*, World Scientific Publishing Co Ltd (1996) pp. 59–81.
- [26] C.T. Bowman, R.K. Hanson, H. Wang, Work presented at the AFOSR/ARO/NSF Basic Combustion Research Reviews, Arlington, VA, June 2-5, 2015 and June 6-10, 2016.
- [27] J. F. Driscoll, Turbulent premixed combustion: Flamelet structure and its effect on turbulent burning velocities, *Prog. Energy Combust. Sci.* 34 (2008) pp. 91–134.
- [28] B. Zhou, C. Brackmann, Q. Li, Z. Wang, P. Petersson, Z. Li, M. Aldén, X.-S. Bai, Distributed reactions in highly turbulent premixed methane/air flames. Part I. Flame structure characterization, *Combust. Flame* 162 (2015) pp. 2937–2953.
- [29] N. Peters, Laminar flamelet concepts in turbulent combustion, *Proc. Combust. Inst.* 21 (1988) pp. 1231–1250.
- [30] N. Peters, The turbulent burning velocity for large-scale and small-scale turbulence, *J. Fluid Mech.* 384 (1999) pp. 107–132.
- [31] K. H. H. Goh, P. Geipel, F. Hampp, R. P. Lindstedt, Flames in fractal grid generated turbulence, *Fluid Dyn. Res.* 45, (2013) 061403.

- [32] K. H. H. Goh, P. Geipel, R. P. Lindstedt, Lean premixed opposed jet flames in fractal grid generated multiscale turbulence, *Combust. Flame* 161 (2014) pp. 2419–2434.
- [33] K. H. H. Goh, P. Geipel, R. P. Lindstedt, Turbulent transport in premixed flames approaching extinction, *Proc. Combust. Inst.* 35 (2015) pp. 1469–1476.
- [34] J. C. Vassilicos, J. C. R. Hunt, Fractal Dimensions and Spectra of Interfaces with Application to Turbulence, *Proc. R. Soc. Lond. A* 435 (1991) pp. 505–534.
- [35] J. Kerl, T. Sponfeldner, F. Beyrau, An external Raman laser for combustion diagnostics, *Combust. Flame* 158 (2011) pp. 1905–1907.
- [36] B. Wieneke, K. Pfeiffer, Adaptive PIV with variable interrogation window size and shape, 15th Int. Symp. Appl. Laser Tech. Fluid Mech. (2010), url: http://ltces.dem.ist.utl.pt/LXLASER/lxaser2010/upload/1845_qkuqls_1.12.3.Full_1845.pdf.
- [37] M. Dunn, A. R. Masri, R. Bilger, R. Barlow, G.-H. Wang, The compositional structure of highly turbulent piloted premixed flames issuing into a hot coflow, *Proc. Combust. Inst.* 32 (2009) pp. 1779–1786.
- [38] B. Zhou, C. Brackmann, Z. Li, M. Aldén, X.-S. Bai, Simultaneous multi-species and temperature visualization of premixed flames in the distributed reaction zone regime, *Proc. Combust. Inst.* 35 (2015) pp. 1409–1416.
- [39] B. Zhou, Q. Li, Y. He, P. Petersson, Z. Li, M. Aldén, X.-S. Bai, Visualization of multi-regime turbulent combustion in swirl-stabilized lean premixed flames, *Combust. Flame* 162 (2015) pp. 2954–2958.
- [40] Y. Minamoto, T. D. Dunstan, N. Swaminathan, R. S. Cant, DNS of EGR-type turbulent flame in MILD condition, *Proc. Combust. Inst.* 34 (2013) pp. 3231–3238.
- [41] J. Savre, H. Carlsson, X. S. Bai, Tubulent methane/air premixed flame structure at high karlovitz numbers, *Flow Turbul. Combust.* 90 (2013) pp. 325–341.
- [42] Y. Minamoto, N. Swaminathan, R. S. Cant, T. Leung, Reaction Zones and Their Structure in MILD Combustion, *Combust. Sci. Technol.* 186 (2014) pp. 1075–1096.
- [43] S.-W. Park, Detailed Chemical Kinetic Model for Oxygenated Fuels, PhD thesis, Imperial College, March 2012, url: <http://hdl.handle.net/10044/1/9599>.
- [44] W. P. Jones, R. P. Lindstedt, The Calculation of the Structure of Laminar Counterflow Diffusion Flames Using a Global Reaction Mechanism, *Combust. Sci. Technol.* 61 (1988) pp. 31–49.

- [45] B. Böhm, C. Heeger, I. Boxx, W. Meier, A. Dreizler, Time-resolved conditional flow field statistics in extinguishing turbulent opposed jet flames using simultaneous high-speed PIV/OH-PLIF, *Proc. Combust. Inst.* 32 (2009) pp. 1647–1654.
- [46] I. G. Shepherd, R. K. Cheng, P. J. Goix, The spatial scalar structure of premixed turbulent stagnation point flames, *Proc. Combust. Inst.* 23 (1991) pp. 781–787.
- [47] A. M. Steinberg, J. F. Driscoll, S. L. Ceccio, Measurements of turbulent premixed flame dynamics using cinema stereoscopic PIV, *Exp. Fluids* 44 (2008) pp. 985–999.
- [48] R. C. Gonzalez, R. E. Woods, S. L. Eddins, *Digital Image Processing Using MATLAB*, New Jersey, Pearson Prentice Hall, 2004.
- [49] V. Giovangigli, M. D. Smooke, Extinction of Strained Premixed Laminar Flames With Complex Chemistry, *Combust. Sci. Techn.* 53 (1987) pp. 23–49.
- [50] U.S. Air Force, Photographic Lenses, Tech. Rep. MIL-STD-150A (1963).
- [51] I. G. Shepherd, J. B. Moss, K. N. C. Bray, Turbulent transport in a confined premixed flame, *Proc. Combust. Inst.* 19 (1982) pp. 423–431.
- [52] G. Hartung, J. Hult, C. F. Kaminski, J. W. Rogerson, N. Swaminathan, *Phys. Fluids* 20 (2008) 035110.
- [53] N. Chakraborty, N. Swaminathan, *Phys. Fluids* 19 (2007) 045103.
- [54] A. M. Steinberg, B. Coriton, J. H. Frank, *Proc. Combust. Inst.* 35 (2015) pp. 1287–1294.
- [55] Y. Gao, N. Chakraborty, N. Swaminathan, *J. Combust.* (2014) 280671.
- [56] P. Petersson, J. Olofsson, C. Brackman, H. Seyfried, J. Zetterberg, M. Richter, M. Aldén, M. A. Linne, R. K. Cheng, A. Nauert, D. Geyer, A. Dreizler, Simultaneous PIV/OH-PLIF, Rayleigh thermometry/OH-PLIF and stereo PIV measurements in a low-swirl flame, *Appl. Optics* 46 (19) (2007) pp. 3928–3936.
- [57] L. W. Kostiuk, K. N. C. Bray, T. C. Chew, Premixed Turbulent Combustion In Counterflowing Streams, *Combust. Sci. Technol.* 64 (4-6) (1989) pp. 233–241.
- [58] C. J. Lawn, R. W. Schefer, Scaling of premixed turbulent flames in the corrugated regime, *Combust. Flame* 146 (2006) pp. 180–199.
- [59] K. A. Buch, W. J. A. Dahm, Experimental study of the fine-scale structure of conserved scalar mixing in turbulent shear flows. Part 2. $Sc = 1$, *J. Fluid Mech.* 364 (1998) pp. 1–29.

- [60] G. K. Batchelor, Small-scale variation of convected quantities like temperature in turbulent fluid Part 1. General discussion and the case of small conductivity, *J. Fluid Mech.* 5 (1959) pp. 113–133.
- [61] R. D. Cook, D. F. Davidson, R. K. Hanson, Shock tube measurements of ignition delay times and OH time-histories in dimethyl ether oxidation, *Proc. Combust. Inst.* 32 (2009) pp. 189–196.
- [62] C. Tang, L. Wei, J. Zhang, X. Man, Z. Huang, Shock Tube Measurements and Modeling Study on the Ignition Delay Times of n-Butanol/Dimethyl Ether Mixtures, *Energy Fuels* 26 (2012) pp. 6720–6728.
- [63] L. Pan, E. Hu, J. Zhang, Z. Zhang, Z. Huang, Experimental and kinetic study on ignition delay times of DME/H₂/O₂/Ar mixtures, *Combust. Flame* 161 (2014) pp. 735–747.
- [64] G. M. Amdahl. Validity of the Single Processor Approach to Achieving Large Scale Computing Capabilities. In AFIPS Spring Joint Computer Conference, 1967. AFIPS 1967 (Spring). *Proc. AFIPS 1967 (Spring)*, 30 (1967) pp. 483–485.
- [65] M. J. Flynn. Some Computer Organizations and Their Effectiveness. *IEEE Transactions on Computers* C-21(9) (1972) pp. 948–960.
- [66] R. Cabra, T. Myhrvold, J. Y. Chen, R. Dibble, A. Karpetis and R. Barlow. Simultaneous laser Raman-Rayleigh-LIF measurements and numerical modeling results of a lifted turbulent H₂/N₂ jet flame in a vitiated coflow. *Proc. Combust. Inst.* 29(2) (2002) pp. 1881–1888.
- [67] R. Cabra. Turbulent Jet Flames Into a Vitiated Coflow. Technical report, NASA, 2004, University of California, Berkeley, California.
- [68] R. Cabra, J. Y. Chen, R. Dibble, A. Karpetis, and R. Barlow. Lifted methane?air jet flames in a vitiated coflow, *Combust. Flame* 143(4) (2005) pp. 491–506.
- [69] R. Cao, S. B. Pope and A. Masri. Turbulent lifted flames in a vitiated coflow investigated using joint PDF calculations, *Combust. Flame* 142(4) (2005) pp. 438–453.
- [70] K. Gkagkas. Flames featuring ignition-extinction: stochastic modelling for the prediction of finite rate chemistry effects, PhD thesis, Imperial College, 2008.
- [71] K. Gkagkas and R. P. Lindstedt. Transported PDF modelling with detailed chemistry of pre- and auto-ignition in CH₄/air mixtures, *Proc. Combust. Inst.* 31(1) (2007) pp. 1559–1566.

-
- [72] K. Gkagkas and R. P. Lindstedt. The impact of reduced chemistry on auto-ignition of H_2 in turbulent flows, *Combust Theory Model.* 13(4) (2009) pp. 607–643.

7 Tables

Tab. 1: Summary of utilised OH intensities ($I_{...}$) for varying fuel and equivalence ratio to define the thresholds $\Lambda_{OH,prod,\Phi}$ and $\Lambda_{OH,str,\Phi}$.

Fluid State	Fluid state normalised signal intensities.				
Φ	0.2	0.4	0.6	0.8	1.0
I^{\ddagger}	1.0				
I_{limit}	≤ 0.5				
I_{HCP}	≤ 2.0				
$I_{BCP,\Phi}$	< 2.0			3.0	3.6
$I_{prod,\Phi}$	1.0 – 2.0	1.0 – 3.0		1.0 – 3.6	
$I_{mild,\Phi}$	> 2.0	2.0 – 3.4	3.0 – 5.6		3.6 – 6.2
$I_{str,\Phi}$	N.A.	≥ 3.4	≥ 5.6	≥ 6.2	
$\Lambda_{OH,prod,\Phi}$	2.0	2.0	2.0	3.0	3.6
$\Lambda_{OH,str,\Phi}$	N.A.	N.A.	3.4	5.6	6.2

Tab. 2: Summary of turbulent and chemical conditions to derive the turbulent Reynolds, Damköhler and Karlovitz numbers for DME/air mixtures at varying Φ and low rate of strain ($a = 75 \text{ s}^{-1}$). The turbulence conditions are evaluated within the reactants. The auto-ignition delay time (τ_{ign}), Da_2 , Ka_2 and Da_3 are evaluated at 1700 K.

Φ	–	0.2	0.4	0.6	0.8	1.0
S_L	m s^{-1}	0.04	0.06	0.21	0.39	0.50
δ_f	mm	1.30	1.09	0.46	0.27	0.24
τ_c	ms	32.5	18.2	2.19	0.69	0.48
τ_{ign}	μs	12.6 ± 0.08				
u_{rms}	m s^{-1}	1.59	1.59	1.59	1.54	1.67
L_I	mm	4.1	4.1	4.1	4.1	4.1
τ_I	ms	2.58	2.58	2.58	2.66	2.46
v_η	m s^{-1}	0.25	0.24	0.23	0.22	0.22
L_η	μm	71	71	73	75	74
τ_η	ms	0.29	0.29	0.31	0.33	0.33
τ_b	ms	8.68				
a_q	s^{-1}	N.A.	N.A.	600	2000	3100
a_T	s^{-1}	4200	4160	3940	3750	3755
ε_r	$\text{m}^2 \text{s}^{-3}$	210	200	173	150	151
$\nu_r \times 10^6$	$\text{m}^2 \text{s}^{-1}$	17.5	17.2	17.0	16.7	16.5
Re_t	–	373	379	383	378	415
Da_1	–	0.08	0.14	1.18	3.86	5.13
Da_2	–	214 ± 13				
Da_3	–	701 ± 42				
Ka_1	–	112	62.8	7.06	2.09	1.45
Ka_2	–	0.046 ± 0.003				

Tab. 3: Summary of utilised OH intensities ($I_{...}$) for DME/air at $\Phi = 0.6$ at varying T_{HCP} to define the thresholds $\Lambda_{OH,prod,T}$ and $\Lambda_{OH,str,T}$.

Fluid State	Fluid state intensities .				
T_{HCP} [K]	1600	1650	1700	1750	1800
$I_{mild,T}$	2.0 – 3.9	2.0 – 3.6	2.0 – 3.3	2.0 – 3.0	2.0 – 2.8
$I_{str,T}$	≥ 3.9	≥ 3.6	≥ 3.3	≥ 3.0	≥ 2.8
$\Lambda_{OH,prod,T}$	2.0	2.0	2.0	2.0	2.0
$\Lambda_{OH,str,T}$	3.9	3.6	3.3	3.0	2.8

Tab. 4: Summary of turbulent and chemical conditions to derive the turbulent Reynolds, Damköhler and Karlovitz numbers for DME/air at $\Phi = 0.6$ at low strain rate ($a = 75 \text{ s}^{-1}$). The turbulence conditions are evaluated within the reactants. The auto-ignition delay time (τ_{ign}), Da_2 , Ka_2 and Da_3 are evaluated at the respective T_{HCP} . The data are supplementary to the data in Table 2.

T_{HCP}	K	1800	1750	1700	1650	1600
τ_{ign}	μs	5.07	6.66	8.96	12.4	17.6
u_{rms}	m s^{-1}	1.63	1.67	1.65	1.60	1.64
ε_r	$\text{m}^2 \text{s}^{-3}$	158	178	172	183	176
Re_t	–	393	403	397	385	395
Da_1	–	1.15	1.12	1.13	1.17	1.14
Da_2	–	495	369	277	206	142
Da_3	–	1712	1303	969	700	493
Ka_1	–	6.67	7.09	6.96	7.19	7.05
Ka_2	–	0.015	0.021	0.029	0.041	0.057

Tab. 5: Physical and resolved length scales in μm . λ_{PIV} and λ_{MF} is the PIV and multi-fluid resolution, respectively. The current minimum laminar flame thickness at $\Phi = 1.0$ is $\min(\delta_f)$. λ_D is the mean scalar dissipation layer thickness [59] and λ_B the Batchelor scale [60].

Scales	Reactants	HCP
λ_{PIV}	300	
λ_{MF}	250	
$\min(\delta_f)$	222	N.A.
λ_D	621 ± 18	N.A.
λ_B	86 ± 15	~ 370

Tab. 6: Multi-fluid interface probabilities for DME/air mixtures in percent by traversing along the stagnation point streamline in 3000 instantaneous images from reactants (R) to products (P). M – mixing fluid, MR – mildly reacting fluid, SR – strongly reacting fluid. Interfaces marked with (–) are not defined.

Interface		Φ				
		0.2	0.4	0.6	0.8	1.0
Samples $\times 10^{-3}$		7.5	7.8	8.8	9.4	9.8
R	M	43	38	36	10	5
R	MR	<1	<1	<1	<1	2
R	SR	–	–	1	10	14
R	P	2	2	1	12	12
M	MR	1	6	8	<1	<1
M	SR	–	–	10	2	1
M	P	39	30	15	8	5
MR	SR	–	–	7	15	18
MR	P	15	24	21	25	27
SR	P	–	–	3	17	15

Tab. 7: Multi-fluid interface probabilities for varying HCP enthalpy in percent by traversing along the stagnation point streamline in 3000 instantaneous images from reactants (R) to products (P). M – mixing fluid, MR – mildly reacting fluid, SR – strongly reacting fluid. Interfaces marked with (–) are not defined.

Interface		T_{HCP} [K]				
		1800	1750	1700	1650	1600
Samples		8953	10018	9489	8349	8390
R	M	20	27	27	31	36
R	MR	6	3	4	4	3
R	SR	8	3	3	2	<1
R	P	10	6	6	6	7
M	MR	3	4	7	9	7
M	SR	7	8	7	4	1
M	P	10	15	13	18	28
MR	SR	6	6	6	4	1
MR	P	22	22	24	22	16
SR	P	8	4	2	1	<1

8 Figures

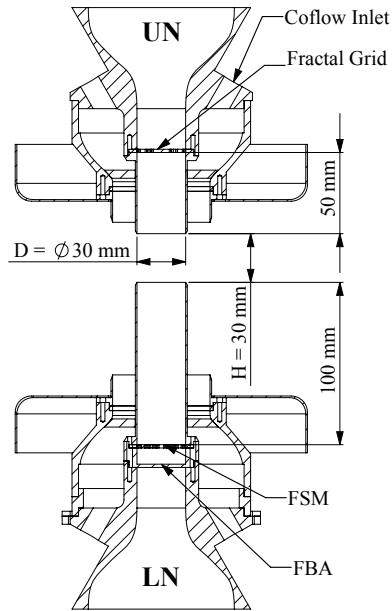


Fig. 1: Experimental configuration.

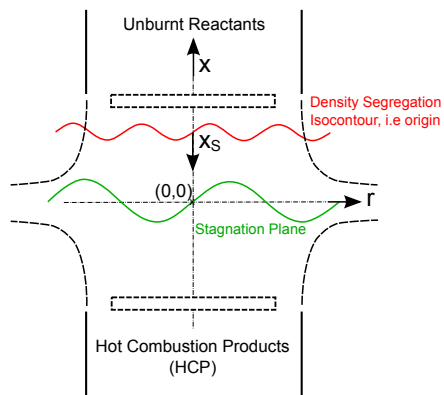


Fig. 2: Coordinate system convention and location of reference windows (dashed rectangles).

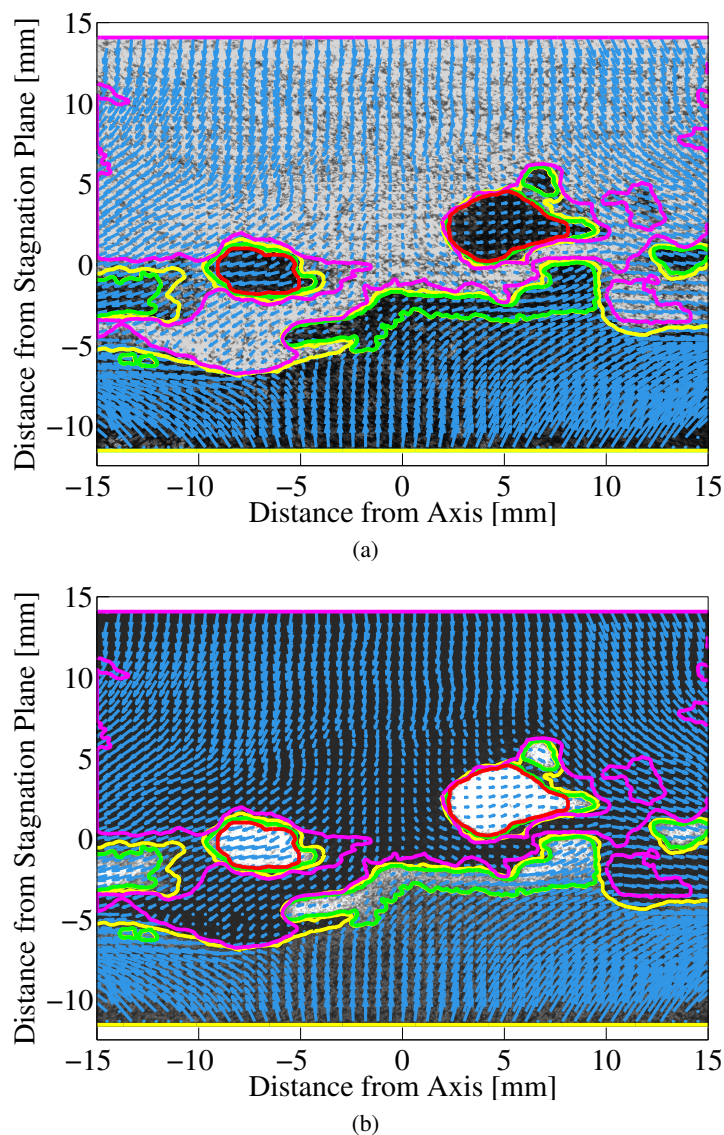


Fig. 3: Identification of the multiple fluid states: (a) Mie scattering; (b) Planar OH LIF image. PIV vectors overlaid. Pink line is the DS iso-contour enclosing the reactant fluid, yellow line encloses the entire OH field, green line encloses the mildly reacting fluid, and red line encloses the strongly reacting (flamelet) fluid. The mixing fluid is bounded between the pink and yellow line.

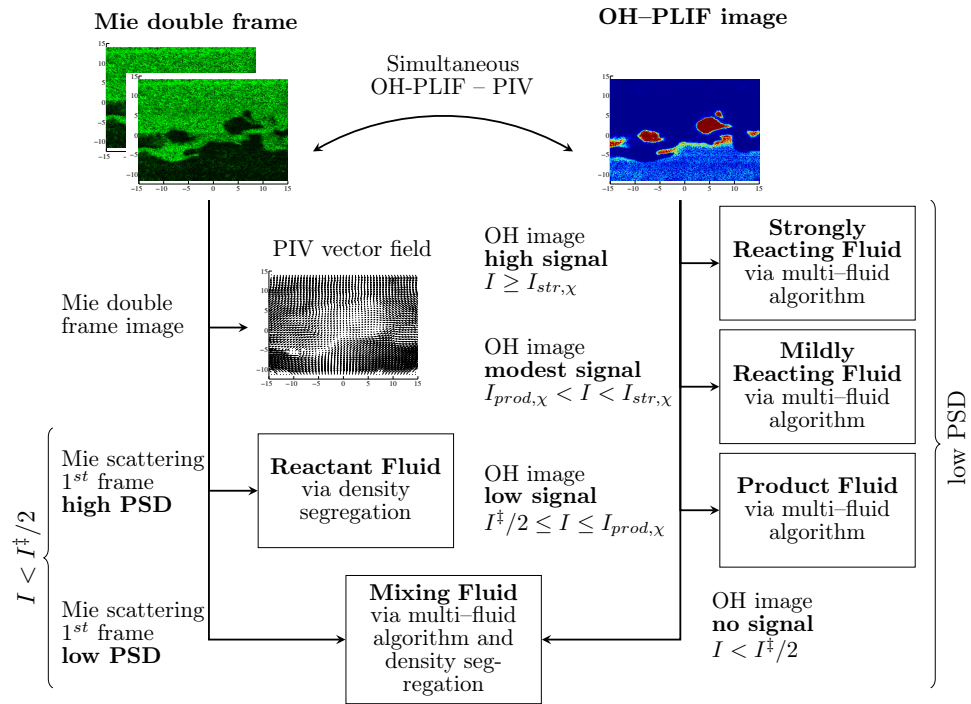


Fig. 4: Schematic visualisation of the multi-fluid post-processing methodology. PSD – particle seeding density; I – experimental OH – PLIF signal intensity.

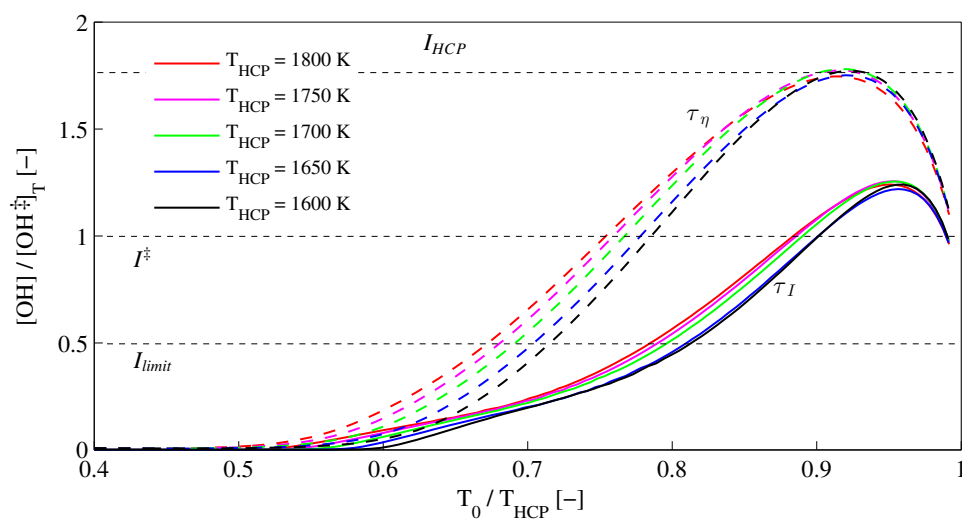


Fig. 5: Perfectly stirred reaction calculations to evaluate the OH concentration following mixing of cold air with HCP at varying T_{HCP} for the integral (τ_I) and Kolmogorov (τ_η) timescale to establish the maximum OH signal level in the absence of fuel.

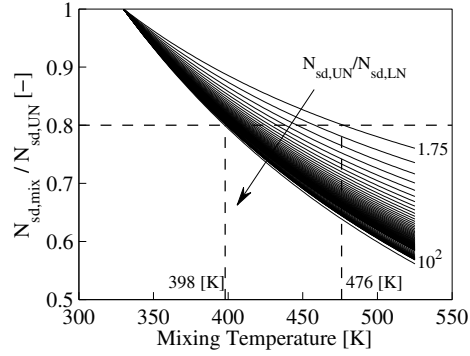


Fig. 6: Theoretical mixture seeding density due to UN and LN stream mixing as a function of blending quantity (i.e. mixing temperature) and seeding density ratio for $T_{HCP} = 1700$ K.

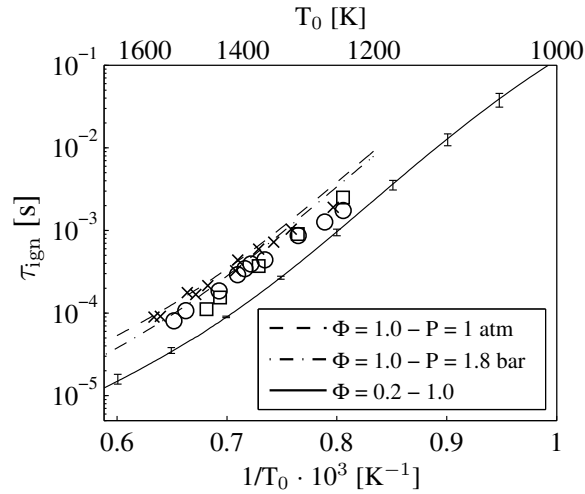


Fig. 7: Perfectly stirred reaction calculations to evaluate auto-ignition delay times for DME-air with the bar representing the variation with $\Phi = 0.2 - 1.0$, $P = 1$ atm and validation calculations at $\Phi = 1.0$, $P = 1.0 - 1.8$ bar with experimental auto-ignition delay times (\square – [61] $\Phi = 1.0$, $P = 1.8$ atm; \bigcirc – [62] $\Phi = 1.0$, $P = 1.0$ bar; \times – [63] $\Phi = 1.0$, $P = 1.2$ atm) for 1 % DME in O_2/Ar mixtures.

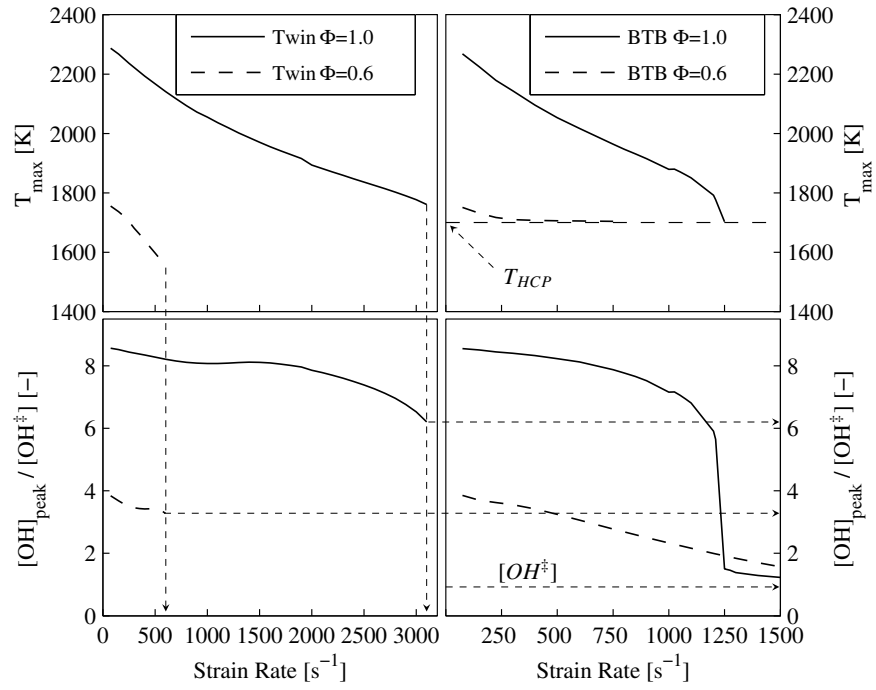


Fig. 8: Laminar flame calculations in a twin (left column) and back-to-burnt (right column) configuration to determine the extinction strain (vertical dashed arrows) and to define the strongly reacting fluid threshold $\Lambda_{OH, str, \Phi}$ (horizontal dashed arrows): 1st row: Maximum temperature; 2nd: Peak OH concentration.

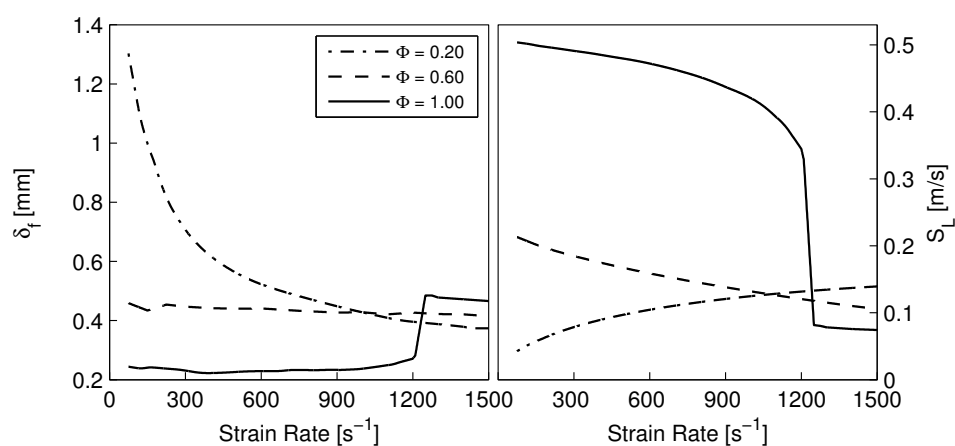


Fig. 9: Laminar flame calculations to visualise the change in burning mode with increasing strain in the back-to-burnt configuration for premixed DME/air flames at varying Φ . Top: Flame thickness δ_f based on the 5 – 95 % of the fuel consumption; Bottom: Laminar burning velocity.

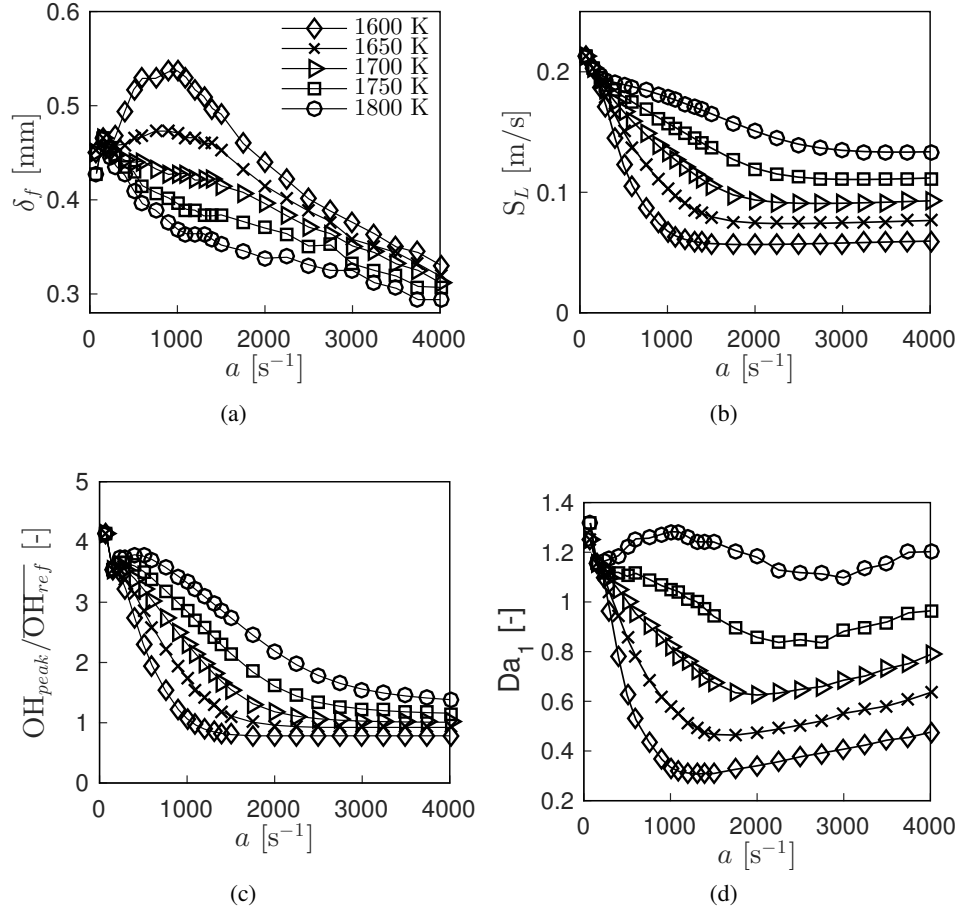


Fig. 10: Laminar flame calculations in a BTB geometry for varying HCP conditions, i.e LHS BC: HCP with T_{HCP} and respective species concentrations; Constant RHS: premixed DME/air at $\Phi = 0.6$ ($\text{Da}_1 = 1.0$). (a) Laminar flame thickness based on the 95 – 5 % fuel consumption; (b) Laminar burning velocity; (c) Normalised OH peak concentration; (d) Damköhler number.

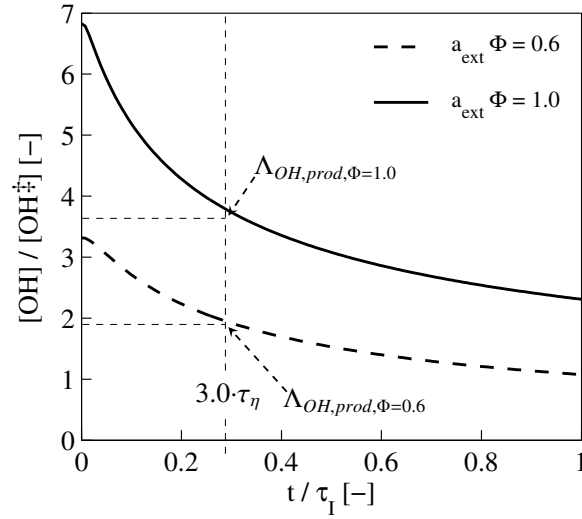


Fig. 11: OH lifetime (t) in the post combustion environment for $\Phi = 0.60$ and 1.00 under extinction conditions. The OH radical drops within $\sim 3.0 \cdot \tau_\eta$ to the OH level of the HCP fluid ($[OH]_{HCP} = 2.0 \cdot OH^\ddagger$) for the case $\Phi = 0.60$ and $\sim 3.6 \cdot OH^\ddagger$ for $\Phi = 1.00$ respectively. The product fluid thresholds ($\Lambda_{OH,prod,\Phi}$) are marked and $\Lambda_{OH,str,\Phi}$ can be inferred at $t / \tau_I = 0$.

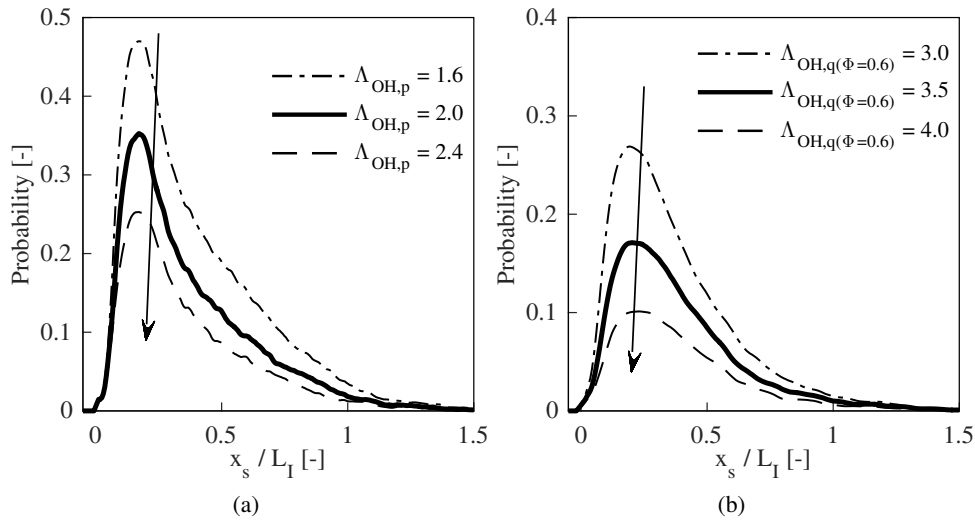


Fig. 12: Sensitivity analysis on thresholds definition: (a) Product fluid threshold ($\Lambda_{OH,prod,\Phi}$) and (b) strongly reacting (flamelet) fluid threshold ($\Lambda_{OH,str,\Phi}$) for $\Phi = 0.6$. Arrows indicate increasing threshold value.

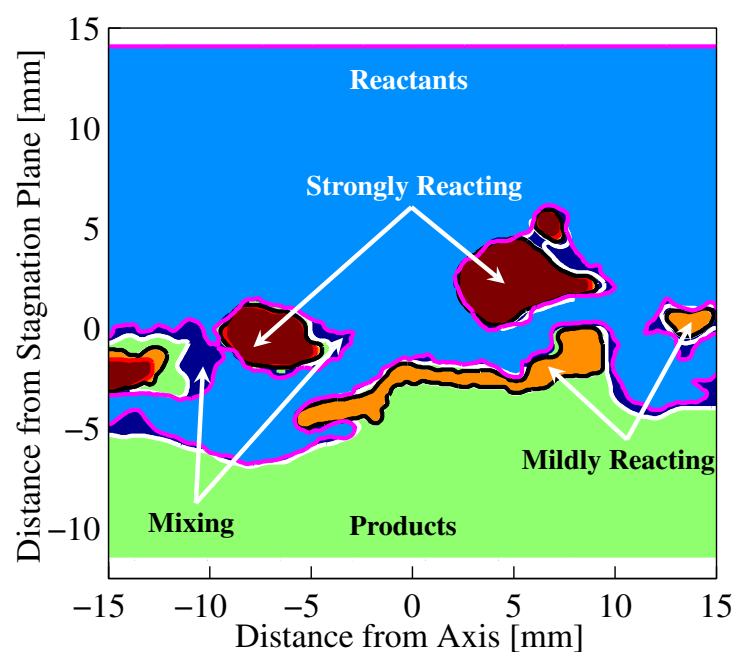


Fig. 13: Example of a quinary multi-fluid field (DME/air – $\Phi = 0.8$): Light blue – **reactant fluid**, dark blue – **mixing fluid**, orange – **mildly reacting fluid**, red – **strongly reacting fluid** and green – **product fluid**. The pink iso-contour encloses the reactant fluid, the white iso-contour encloses all OH signal, the black iso-contour encloses the mildly reacting fluid, the red iso-contour encloses the strongly reacting (flamelet) fluid and the mixing fluid is bordered by the pink and white iso-contour.

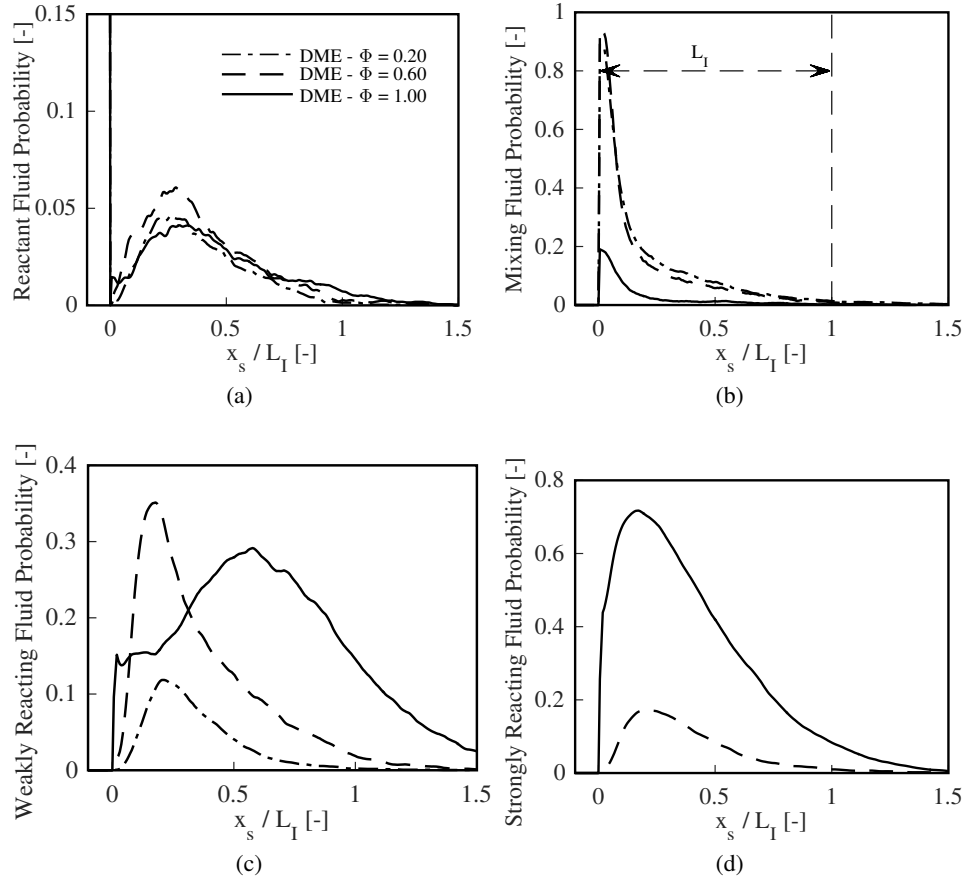


Fig. 14: Multi-fluid probability statistics for DME cases at $\Phi = 0.2 - 1.0$ and aligned at the first thermal alteration iso-contour: (a) Reactant fluid; (b) Mixing fluid; (c) Mildly reacting fluid; (d) Strongly reacting (flamelet-like) fluid probability. The markers on the DME - $\Phi = 0.20$ line are drawn for identification purposes and do not represent the actual resolution.

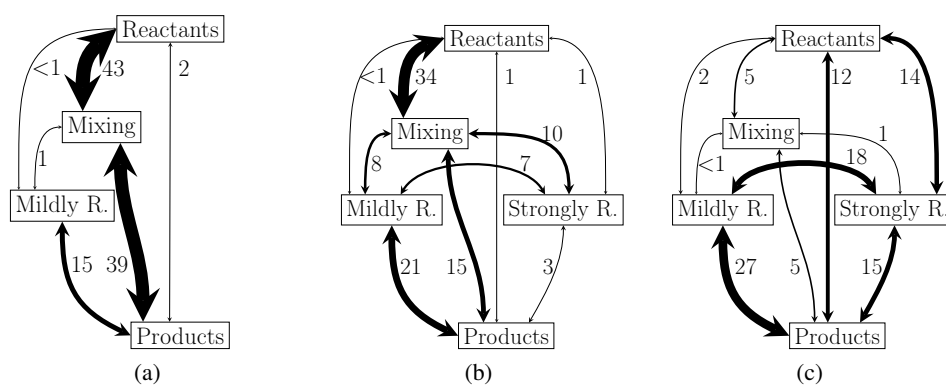


Fig. 15: Multi-fluid interface diagram for DME/air mixtures at $\Phi = 0.2$ (left), $\Phi = 0.6$ (middle) and $\Phi = 1.0$ (right) and elaborated for all cases in Table 6. The distinct shift towards higher reactive and more exothermic intermediate fluid states is illustrated by means of the probability weighted arrows, indicating adjacent fluid states.

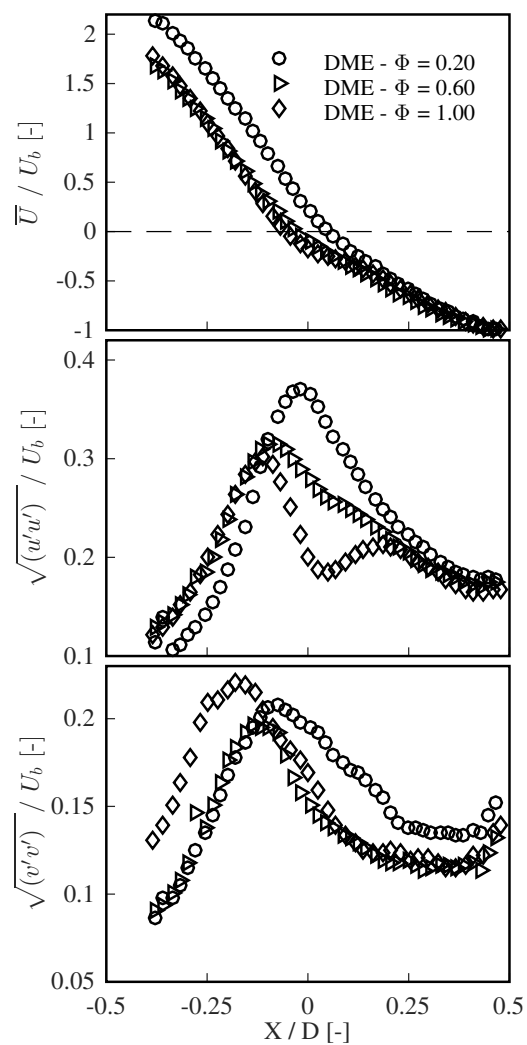


Fig. 16: Unconditional velocity and its fluctuation along the stagnation point streamline: Mean axial velocity (top row), axial velocity fluctuation (middle row) and radial velocity fluctuation (bottom row). Only every second data point is drawn to enhance the readability.

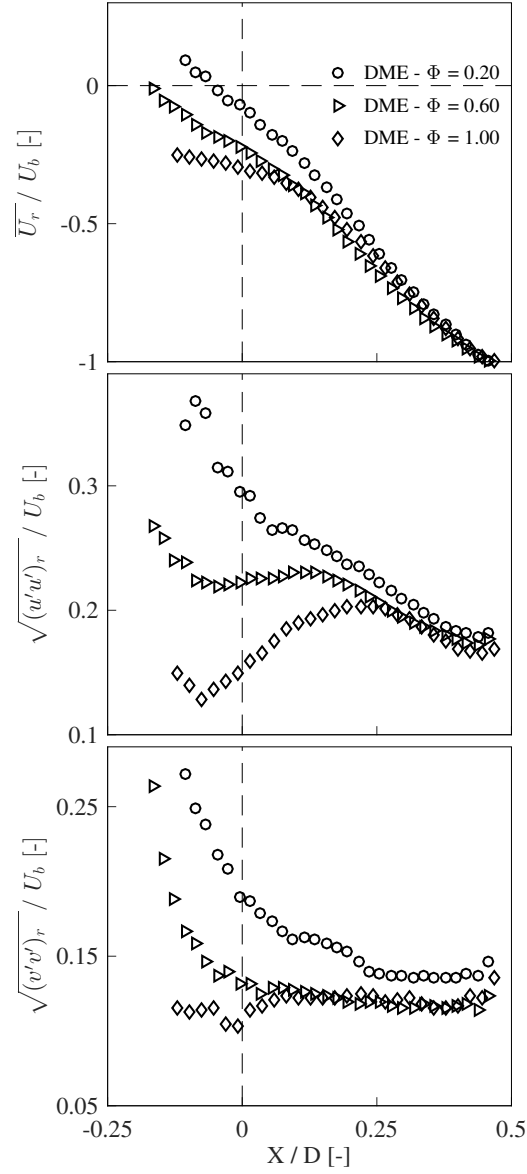


Fig. 17: Conditional mean axial reactant fluid velocity and fluctuations along the stagnation point streamline: Top - $\overline{U_r}/U_b$; Middle - $\sqrt{(u'u')_r}/U_b$; Bottom - $\sqrt{(v'v')_r}/U_b$.

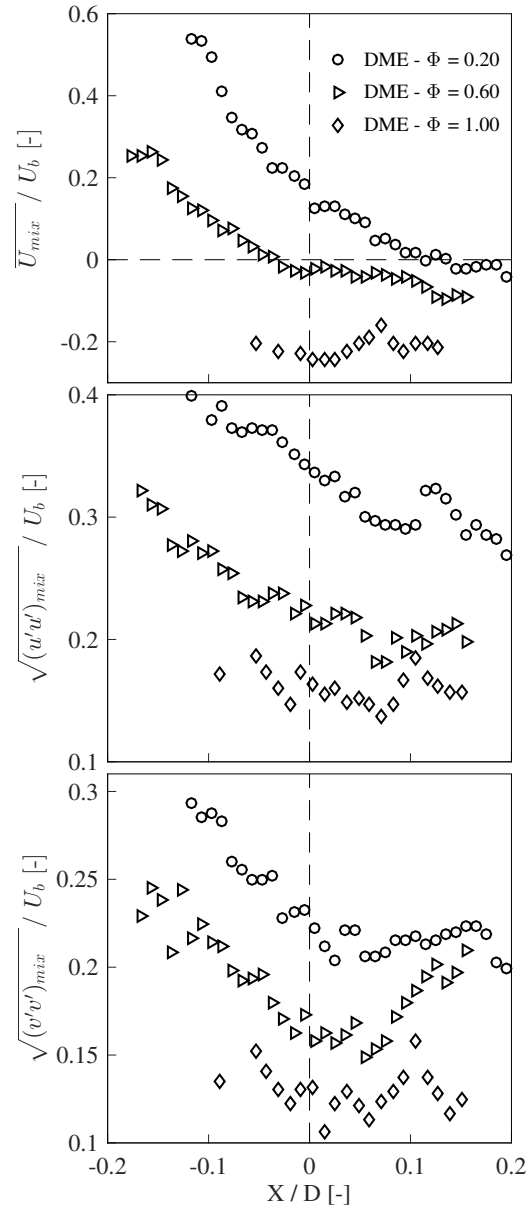


Fig. 18: Conditional mean axial mixing fluid velocity and fluctuations along the stagnation point streamline: Top – $\overline{U_{mix}}/U_b$; Middle – $\sqrt{(u'u')_{mix}}/U_b$; Bottom – $\sqrt{(v'v')_{mix}}/U_b$.

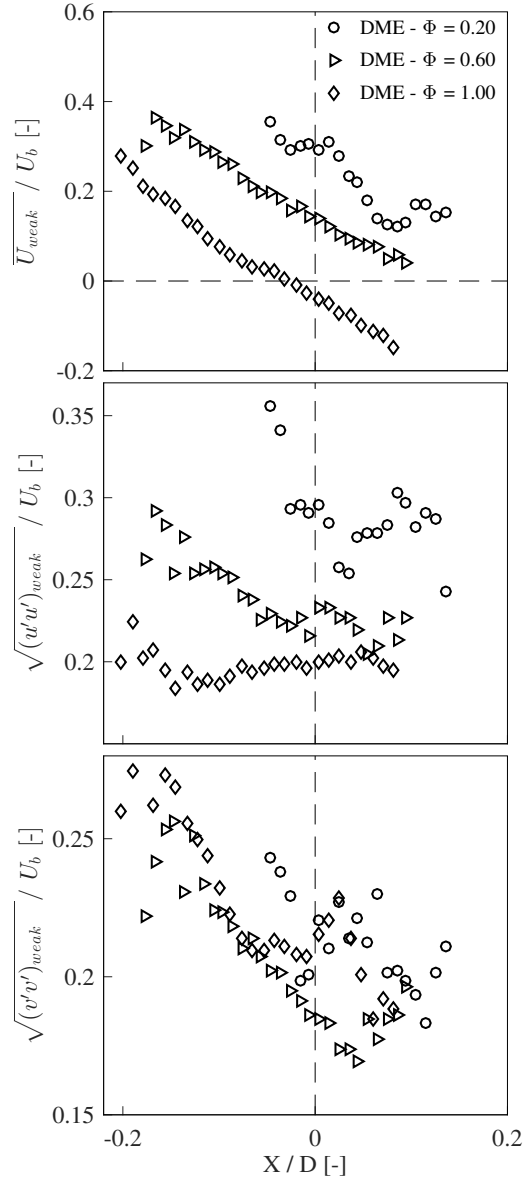


Fig. 19: Conditional mean axial mildly reacting fluid velocity and fluctuations along the stagnation point streamline: Top - $\overline{U_{mild}}/U_b$; Middle - $\sqrt{(u'u')_{mild}}/U_b$; Bottom - $\sqrt{(v'v')_{mild}}/U_b$.

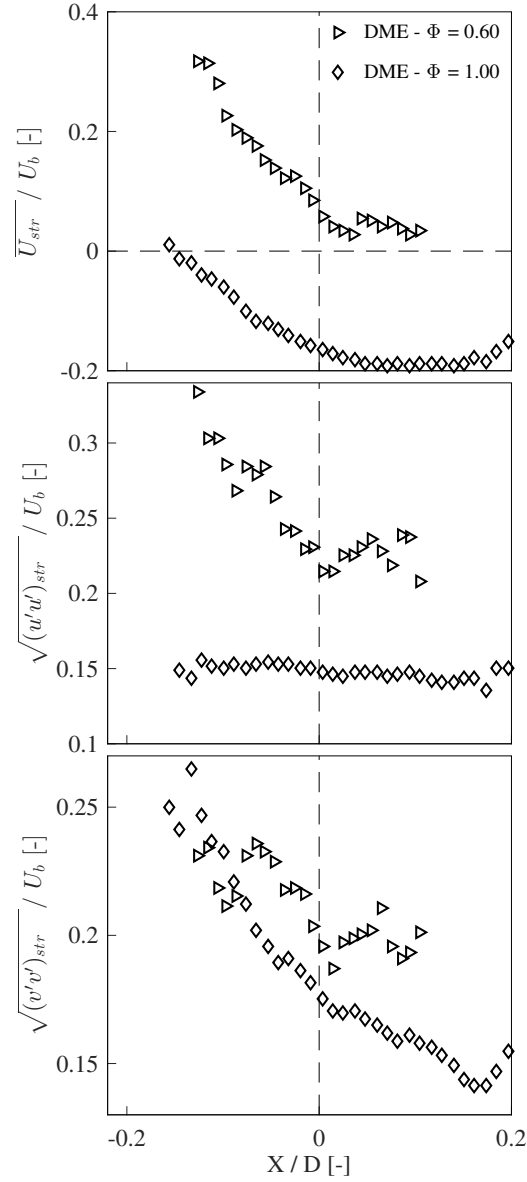


Fig. 20: Conditional mean axial strongly reacting fluid velocity and fluctuations along the stagnation point streamline: Top – $\overline{U_{str}}/U_b$; Middle – $\sqrt{(u'u')_{str}}/U_b$; Bottom – $\sqrt{(v'v')_{str}}/U_b$.

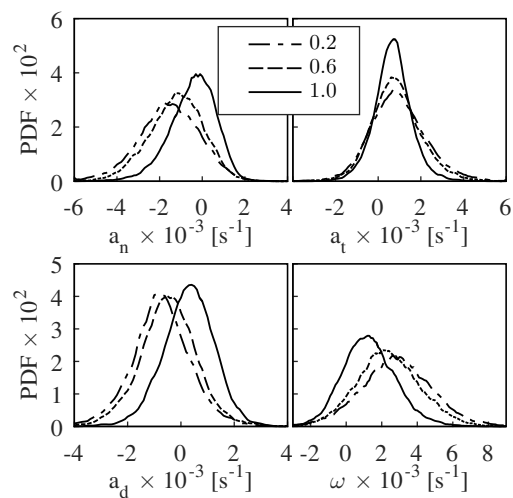


Fig. 21: PDF of the rate of strain and vorticity evaluated along the reactant fluid surface: Top left: Normal strain; Right: Tangential strain; Bottom left: Total strain; Right Vorticity. Legend refers to Φ .

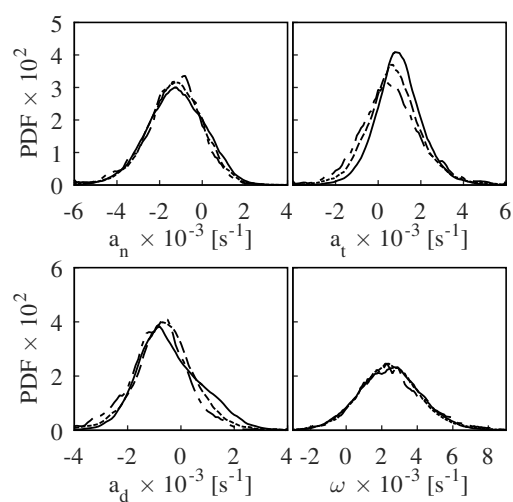


Fig. 22: PDF of the rate of strain and vorticity evaluated along the mildly reacting fluid surface: Top left: Normal strain; Right: Tangential strain; Bottom left: Total strain; Right Vorticity. Legend identical to Fig. 21.

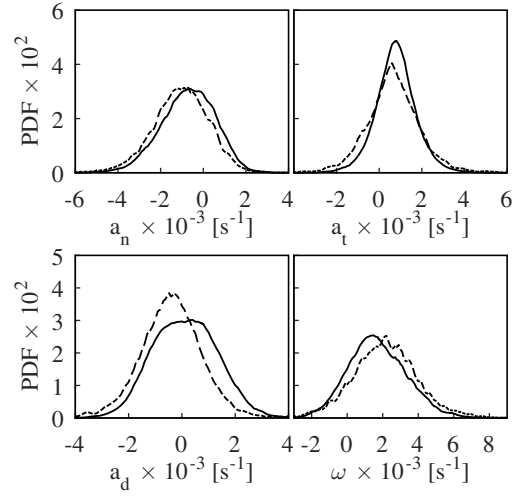


Fig. 23: PDF of the rate of strain and vorticity evaluated along the strongly reacting fluid surface: Top left: Normal strain; Right: Tangential strain; Bottom left: Total strain; Right Vorticity. Legend identical to Fig. 21.

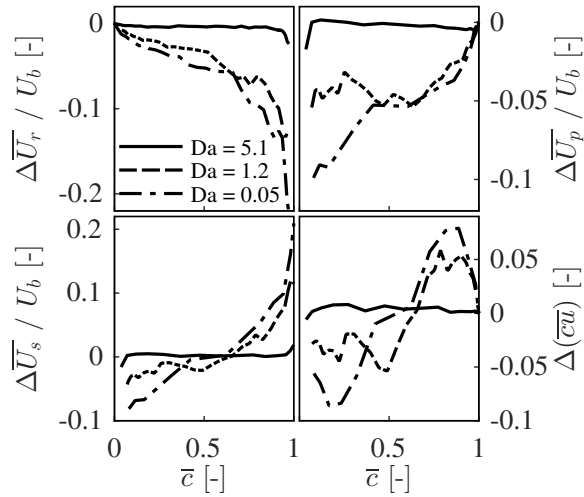


Fig. 24: Limitation of a bimodal description evaluated by the difference (Δ) between a particle density and OH signal based segregation technique along the reaction progress \bar{c} . Discrepancy of the mean axial reactant fluid (top left), product fluid (top right) and slip (bottom left) velocity as well as scalar flux (bottom right).

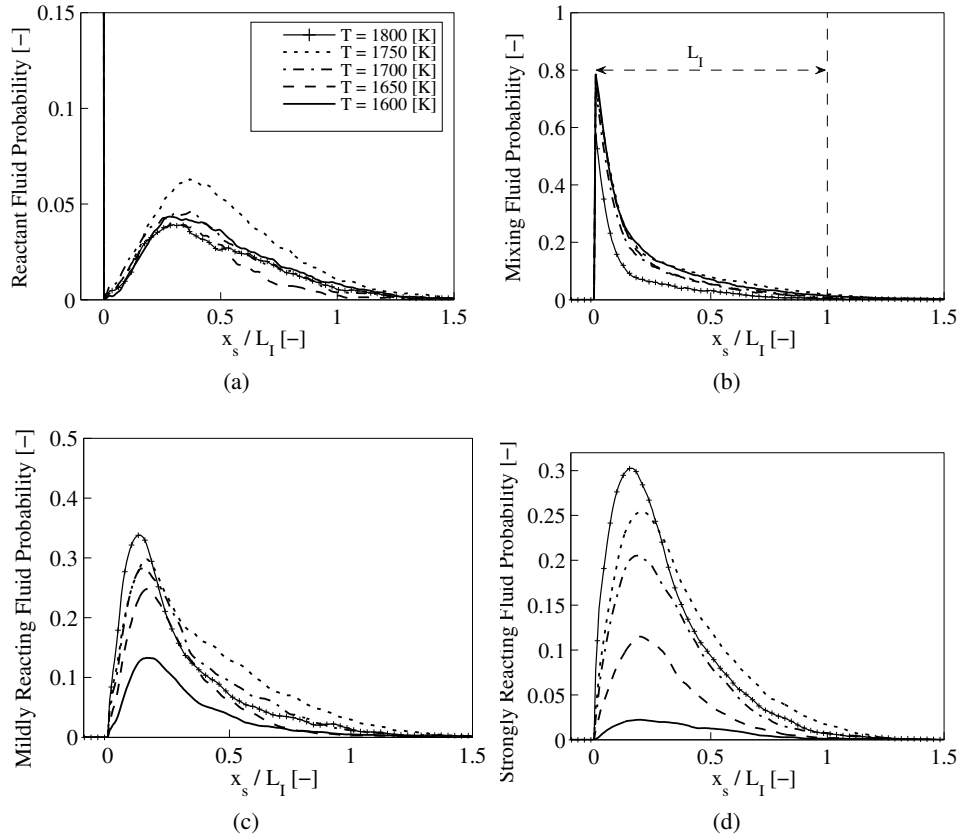


Fig. 25: Multi-fluid probability for DME cases at $\Phi = 0.6$ with $T_{HCP} = 1600 - 1800$ K: (a) Reactant fluid; (b) Mixing fluid; (c) Mildly reacting fluid; (d) Strongly reacting (flamelet-like) fluid probability. The markers are drawn for identification purposes and do not represent the actual resolution.

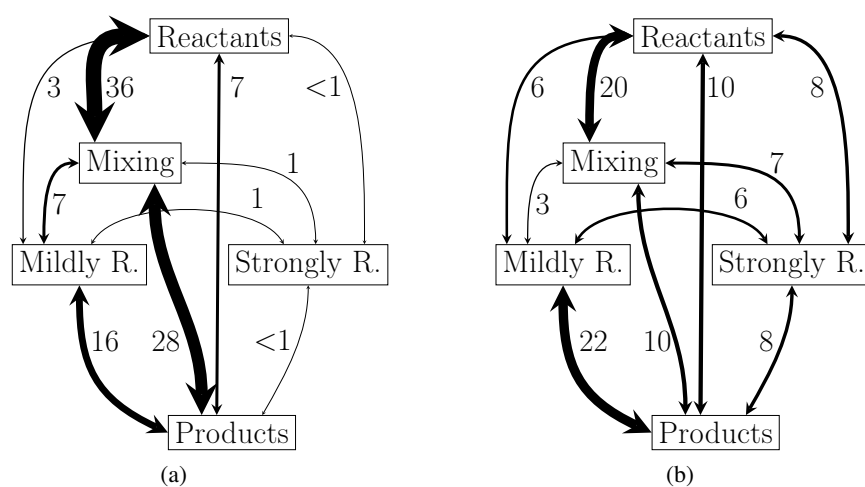


Fig. 26: Multi-fluid interface diagram for DME / air at $\Phi = 0.6$ and a supporting HCP temperature of: (a) $T_{HCP} = 1600$ and (b) 1800 K. A shift towards higher HCP blending fraction for reduced HCP enthalpy is required to initialise OH producing chemical activity with absolute interface probabilities listed in Table 7.

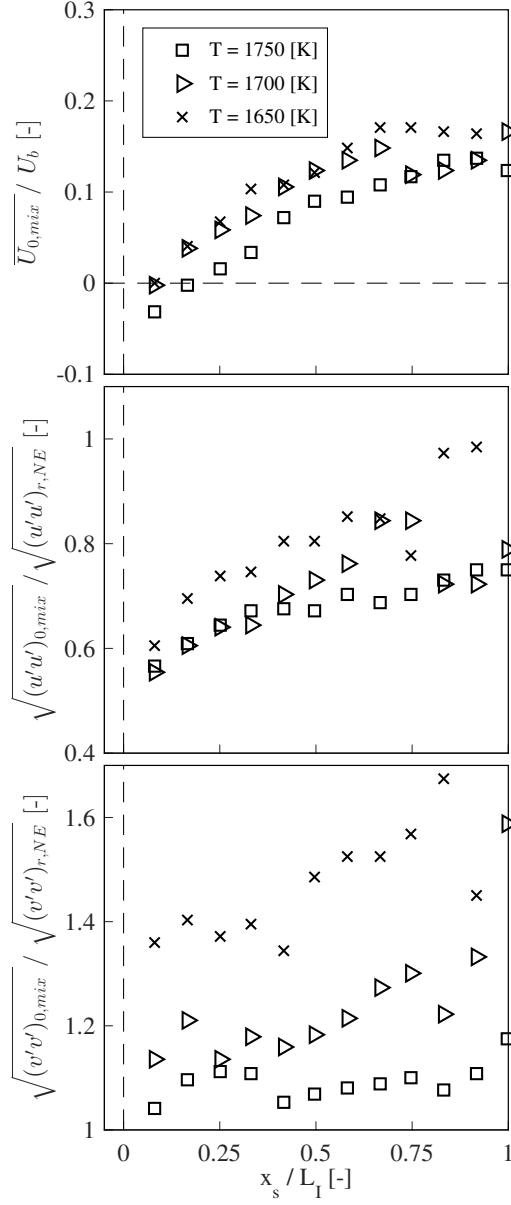


Fig. 27: Conditional mean axial mixing fluid velocity and fluctuations along the stagnation point streamline and aligned at the Mie scattering iso-contour ($x_s = 0$): Top – $\overline{U_{0,mix}}/U_b$; Middle – $\sqrt{(u'u')_{0,mix}}/\sqrt{(u'u')_{r,NE}}$; Bottom – $\sqrt{(v'v')_{0,mix}}/\sqrt{(v'v')_{r,NE}}$.

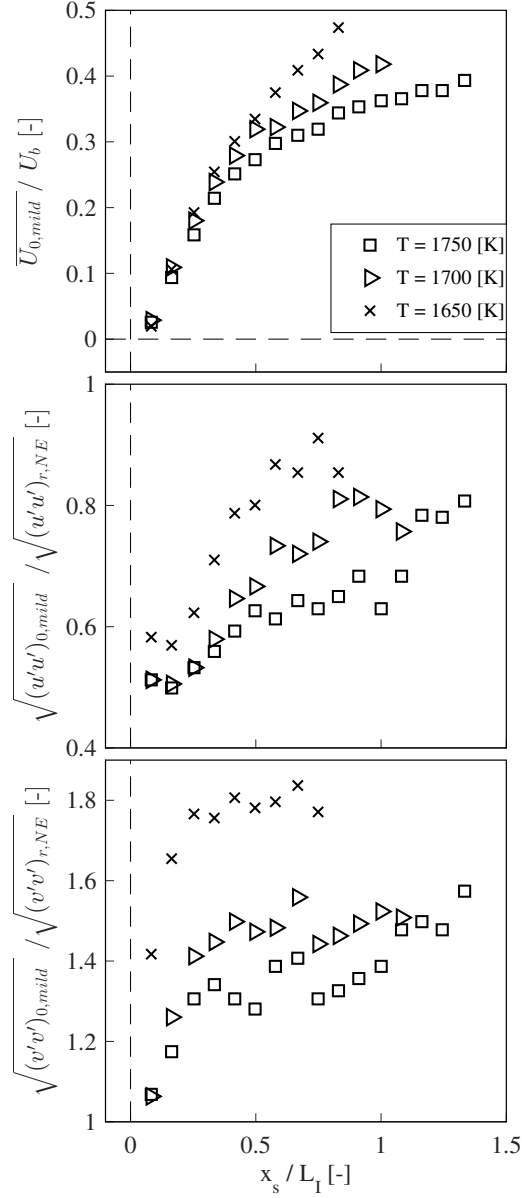


Fig. 28: Conditional mean axial mildly reacting fluid velocity and fluctuations along the stagnation point streamline and aligned at the Mie scattering iso-contour ($x_s = 0$): Top – $\overline{U_{0,mild}} / U_b$; Middle – $\sqrt{(u'u')_{0,mild}} / \sqrt{(u'u')_{r,NE}}$; Bottom – $\sqrt{(v'v')_{0,mild}} / \sqrt{(v'v')_{r,NE}}$.

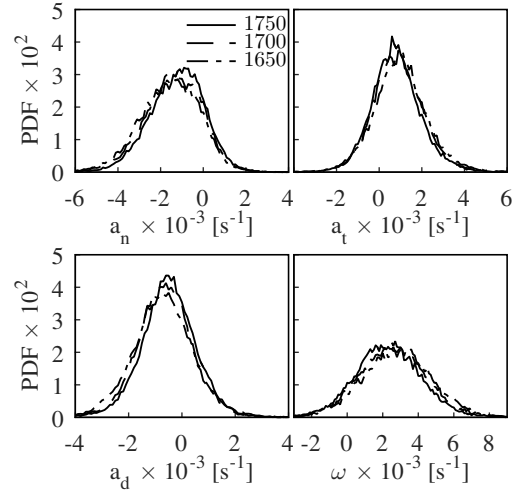


Fig. 29: PDF of the rate of strain and vorticity evaluated along the reactant fluid iso-contour: Top left: Normal strain; Right: Tangential strain; Bottom left: Total strain; Right Vorticity.

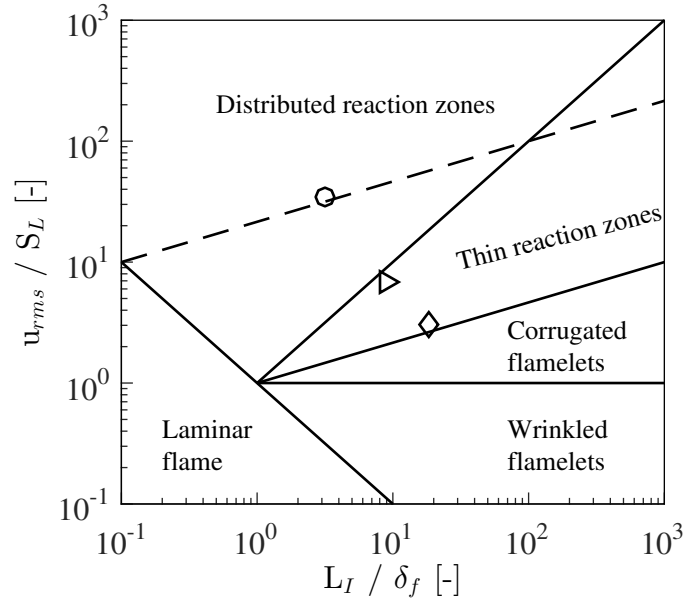


Fig. 30: Combustion regime transitions of DME/air mixtures at varying Φ visualised in a Borghi diagram. Symbols as in Figs. 16 – 20.

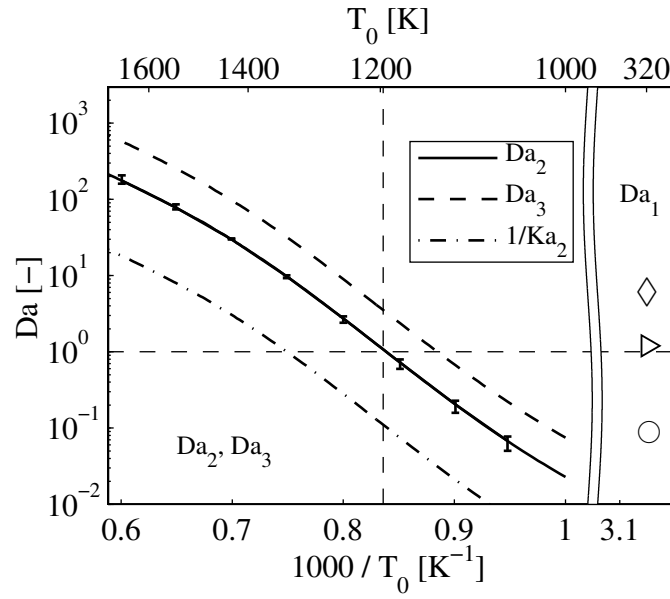


Fig. 31: Auto-ignition manifold for DME/air mixtures with Damköhler numbers based on the turbulent integral timescale (Da_2), the bulk flow timescale (Da_3) and the inverse of the auto-ignition Karlovitz number ($1/Ka_2$) as a function of initial temperature (T_0). The conventional Da_1 for the different equivalence ratios (symbols as in Figs. 16 – 20) are also shown at $T_0 = 320$ K. The bars on the Da_2 line indicate the mixture impact ($\Phi = 0.2 - 1.0$).

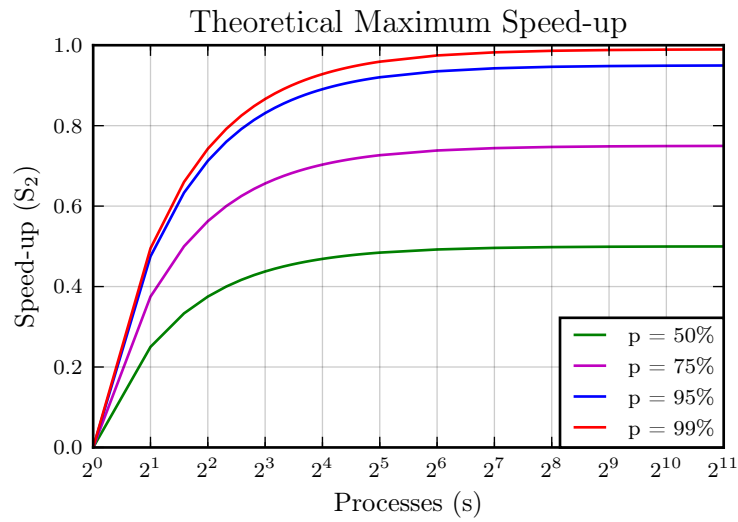


Fig. 32: The theoretical maximum speed-up according to Amdahl's Law [64].

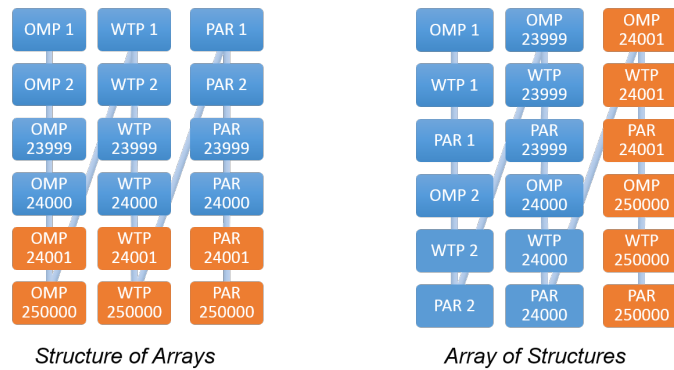


Fig. 33: The difference in memory alignment of a Structure of Arrays and Arrays of Structures.

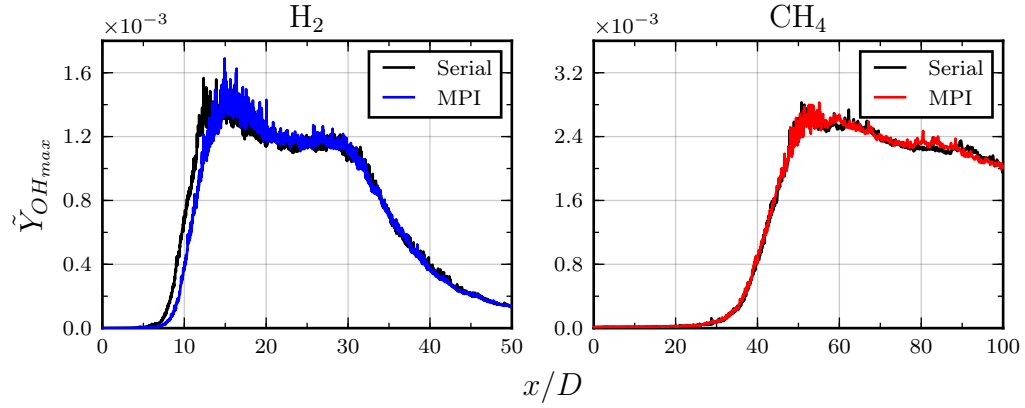


Fig. 34: Comparing the maximum OH concentrations obtained with the serial version of PIPER and that parallelised using MPI. The left figure was obtained with a detailed mechanism for a H_2 flame and the right figure with a detailed mechanism for the corresponding CH_4 flame.

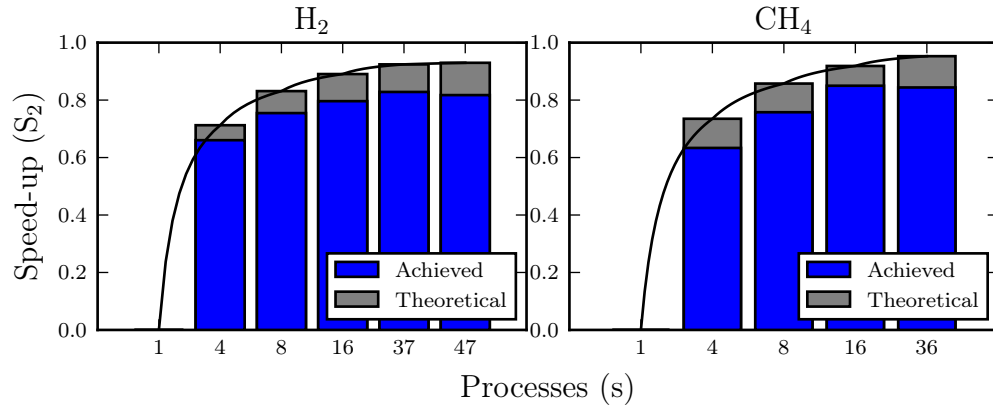


Fig. 35: The achieved speed-up of PIPER using MPI. The left figure feature a detailed mechanism for H_2 and the right figure the detailed mechanism for the corresponding CH_4 flame. The tail-off in gain is due to the small domain size (number of computational cells used).